T · H · E
OHIO STATE UNIVERSITY

Supersonic Combustion Engine Testbed, "Heat Lightning"

Student Authors: D. Hoying, C. Kelble, A. Langenbahn, M. Stahl, M. Tincher, M. Walsh, and S. Wisler

Supervisor: Dr. G. M. Gregorek
Assistant: R. L. Reuss
Department of Aeronautical & Astronautical Engineering

Supersonic Combustion Engine Testbed, "Heat Lightning"

Student Authors: D. Hoying, C. Kelble, A. Langenbahn, M. Stahl, M. Tincher, M. Walsh, and S. Wisler

Supervisor: Dr. G. M. Gregorek
Assistant: R. L. Reuss
Department of Aeronautical & Astronautical Engineering

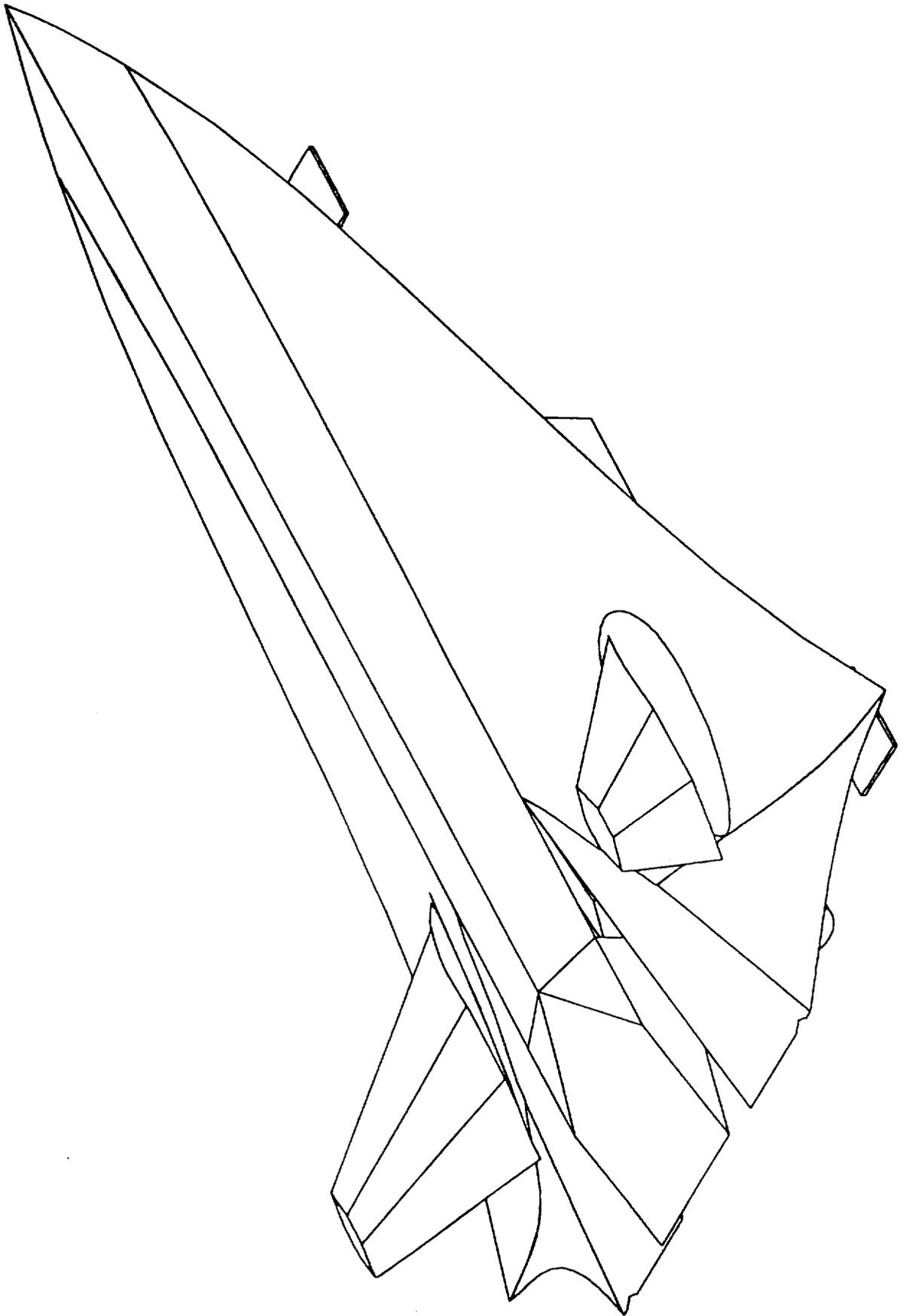# Supersonic Combustion Engine Testbed

"Heat Lightning"

Aircraft Design Case Study

AAE 416 Advanced Hypersonic Design Course

Red Team
Don Hoying
Chris Kelble
Andy Langenbahn
Maria Stahl
Melissa Tincher
Mike Walsh
Scott Wisler

Acknowledgements

We would like to express our appreciation to Professor Gerald M. Gregorek and Teaching Assistant Robyn Reuss for providing the inspiration and direction necessary to complete this project. We would also like to thank the individuals at NASA and the USRA whose funding made this project possible. Thanks also to General Electric Aircraft Engines for providing valuable engine data. We have benefitted from the experience provided by Bob Boyd, Tom Ramsey, and Phil Weissman. Additionally, we would like to thank Dave Miklosovic for the help he provided with solid computer modeling of our aircraft.

Abstract

Supersonic combustion ramjet (SCRAMjet) engines will be required to power next generation aircraft having flight velocities above Mach 6. These engines will require extensive flight testing to evaluate installed performance, efficiency, and safety. The Supersonic Combustion Engine Testbed (SCET) aircraft has been designed to test SCRAMjet engines using a minimum drag, Mach 10 optimized waverider. This aircraft will launch from a carrier aircraft and accelerate to SCRAMjet engine operating conditions using turbofan-ramjet engines. Flight between Mach 6 and 10 will be powered by the SCRAMjet engines. The design of this aircraft provided many obstacles in aerodynamics, materials technology, and systems integration. While some of the necessary technologies have not matured yet, all of the basic technology currently exists. Provided sufficient emphasis and funding, we believe a first flight in the year 2000 is possible.

Table of Contents

List of Figures

List of Tables

Section 1: Introduction

Aerospace applications place the highest demands on our understanding in technical areas such as materials, computational methods, and thermochemistry. The production of the Supersonic Combustion Engine Testbed (SCET) provides great challenges in all of these areas. Many of the technical capabilities do not yet exist to produce such an aircraft. The development of this capability, however, is the purpose of the SCET program.

Supersonic Combustion Ramjets (SCRAMjets) are currently being tested in laboratories. Solutions to the viscous Navier-Stokes equations are now possible for simple shapes using Computational Fluid Dynamics. And, high temperature, high strength composites are steadily extending the limits where materials can survive. These new and exciting technologies make the SCET a possibility. The need for further development and proof of these technologies may make it a necessity.

A number of these technologies are maturing at the same time (and not by chance) to make hypersonic flight using air breathing propulsion a possibility. Without near term programs such as the SCET, progress on these technologies may stagnate. This can not be allowed to happen. It is imperative that the nineties make a more substantial contribution to hypersonic flight than did the sixties if progress is to continue into the twenty-first century.

Section 2: Design Goals

2.1 Design Criteria:

A list of design criteria were presented to the group at the beginning of this design project. They are as follows:

- Piloted aircraft.
- Launched at M = 0.8, 40,000 feet altitude from a carrier aircraft.
- Capable of accelerating to M = 6.0.
- Continue accelerating to M = 10.0, 100,000 feet using a prototype SCRAMjet engine.
- Cruise at M=10.0 for two minutes.
- Land at Dryden Flight Test Center, CA.
- Maximum weight of 75,000 lb.

It is not always possible, however, to view all design criteria as absolute. Some criteria may end up in conflict or simply impractical when viewed against the other items. Therefore, it is necessary to evaluate the fundamental goal of the mission. From this fundamental goal, the initial criteria can be evaluated, and other goals can be determined. For this project, the most fundamental goal was determined to be the test of the experimental SCRAMjet engine. Additionally, it is necessary to remain under 75,000 pounds to remain compatible with the drop aircraft. If other design criteria could be modified to enhance the achievement of this basic goal it would be done. However, it is intended to adhere to all of these design criteria if

possible. They will be used as the starting point in all cases. From the fundamental goal, other criteria can be imposed such as the following:

- Integration of the SCRAMjet should take precedence over the installation of other systems.

- The choice of fuel will be dictated by the SCRAMjet to avoid multiple fuel systems.

- Sufficient fuel must remain for meaningful SCRAMjet testing following acceleration to M=6.0 to consider the design successful.

- Low maintenance requirements on systems to reduce turn around time.

Together, all of these criteria and goals provide the yard stick used to measure the success of the program.

2.2 Why a Pilot:

One of the most basic design criteria worth evaluating is the need for a pilot within the aircraft. Physically, placing a pilot within the aircraft is not difficult. However, it does increase both the size and cost of the aircraft somewhat. Yet, a pilot does offer some distinct advantages. There are two categories of arguments in support of a piloted aircraft of this type. The first category, mission critical, contains two arguments. There will be points in the flight where loss of communication could occur due to ionization. It would be advantageous to have a pilot in the aircraft at these points

rather than rely on pre-programmed instructions. In addition to ionization, a pilot could be vital to the success of the mission and the survival of the aircraft if something unforseen occurs. The second category, research, also contains two arguments. The first is simple: a pilot would allow variability in the test. He/she would allow the aircraft to be used for different types of test without large changes to the control program of the aircraft. Finally, the aircraft would provide human factors data. The concept for an aircraft such as the National Aerospace Plane (NASP) is already in the works. The NASP will not only have a pilot, it will also transport people. The development of a flight control system for such an aircraft must allow for the physiological as well as psychological reactions of the pilot to be successful and safely integrated with the capabilities of the plane.

Section 3: Configuration

3.1 Waverider Concept:

What is a waverider? The waverider is formed from the known flow field of a shock wave. When a waverider is travelling at its design Mach number, the shock is attached to the leading edges of the body (Figure 3.1). Since the shock is attached, there is no flow spillage from the lower to upper surface. Thus, high pressure is trapped on the lower surface resulting in efficient lift. The waverider is so named because it appears to be riding on top of the attached shock wave.

Figure 3.1: Waverider Theory

CONSTRUCTION FROM KNOWN FLOW FIELD

RESULTING WING AND SHOCK
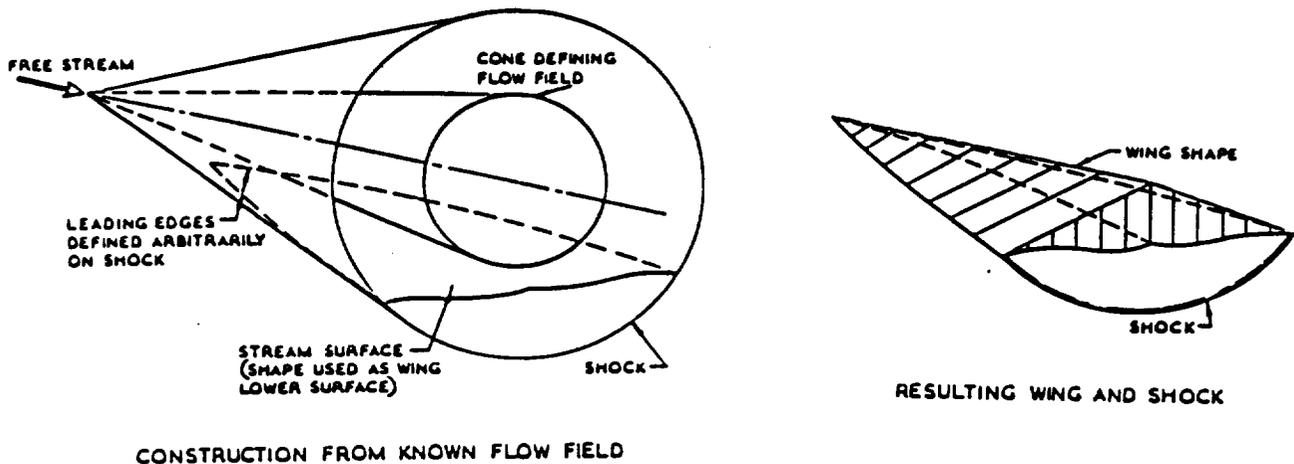
A program called MAXWARP was developed by Stephen Corda and John Anderson at The University of Maryland which outputs the geometry of a waverider body given the Mach number and a few size constraints. Also included in the program was a routine to optimize for maximum lift to drag or for minimum drag. For this

5

case, the program was used to optimize for minimum drag. This was chosen since this aircraft would spend a relatively small amount of time at cruise conditions.

A configuration was needed which could perform well at varying Mach numbers. Since the MAXWARP program could only be run for a given design Mach number, it remained to be proved that the waverider could perform reasonably well at off design conditions. The MAXWARP program was run at Mach numbers of 6, 8 and 10 to see how the geometry changed for a given Mach number (Figure 3.2). Although the front views were somewhat different, the top view (planform) for each Mach number was very similar. The concept of the waverider depends mostly upon the shape of the planform. Therefore, the off design performance was considered adequate for the mission. In addition, the results of a study conducted at the University of Maryland confirmed the assumption that the waverider performed adequately at off design conditions.

Figure 3.2: Waverider Comparison

Mach = 10.0   Mach = 8.0   Mach = 6.0
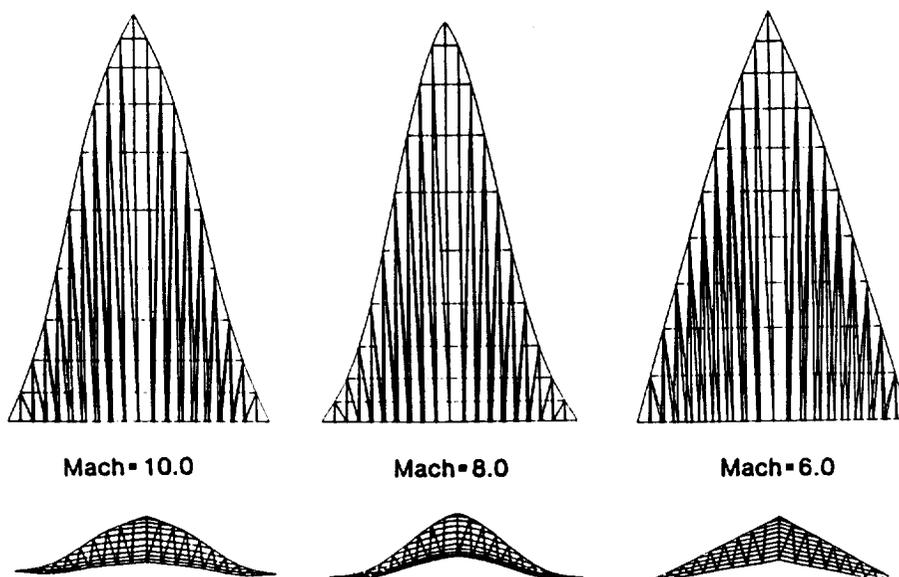
The main advantages to using the waverider configuration were drag considerations and fuel and engine integration. The waverider configuration made the integration of a small cockpit, multiple engines, and fuel easier than would a conventional fuselage/wing design. Optimizing for minimum drag helped to reduce the total fuel requirements by reducing the thrust needed for the flight profile.

3.2 Systems Integration:

Once the general body shape was chosen to be that of a waverider, the task remained of integrating the engine systems, fuel systems, and the cockpit into the body. A number of configurations were tried in an attempt to optimize the use of available internal volume while minimizing drag increases.

Four SCRAMjet modules were needed to provide the necessary thrust. The easiest way to combine these modules was to place them side by side. It was decided that the middle section of the bottom of the aircraft would be used for the SCRAMjet engines. Doing this allows the front underside of the aircraft to be used as part of the inlet. This also places the engines near the centerline in case of engine failure. A boat tail was added to the rear of the aircraft to allow more exhaust expansion.

The biggest problem faced with the configuration was the integration of the turbofan-ramjets and fuel tanks. These engines are very long and large in diameter making them difficult to integrate with the body of the waverider. To minimize drag,

the engines should be internalized as much as possible. They should also be placed close to the centerline if possible so that control could be maintained in an engine-out situation. Another problem, however, was keeping the hydrogen stored in the coolest possible areas. This area is in the thickest portion of the aircraft near the tail. In addition, the hydrogen must be stored under high pressure, which means the tanks should use simple geometry.

Once the waverider data became available, it was discovered that the waverider body was much thinner than anticipated. This presented two problems: one, the engines could only be completely internal if placed along the centerline as far back as possible, and two, the volume available for fuel storage decreased significantly. The decision, therefore, was to move the engines away from the centerline and allow them to protrude from the aircraft. This meant paying a control and drag penalty, but the centerline of the aircraft would then be available for fuel volume (see Figure 3.3).

Figure 3.3: Internal Systems 4-View

COCKPIT

FUEL CELLS
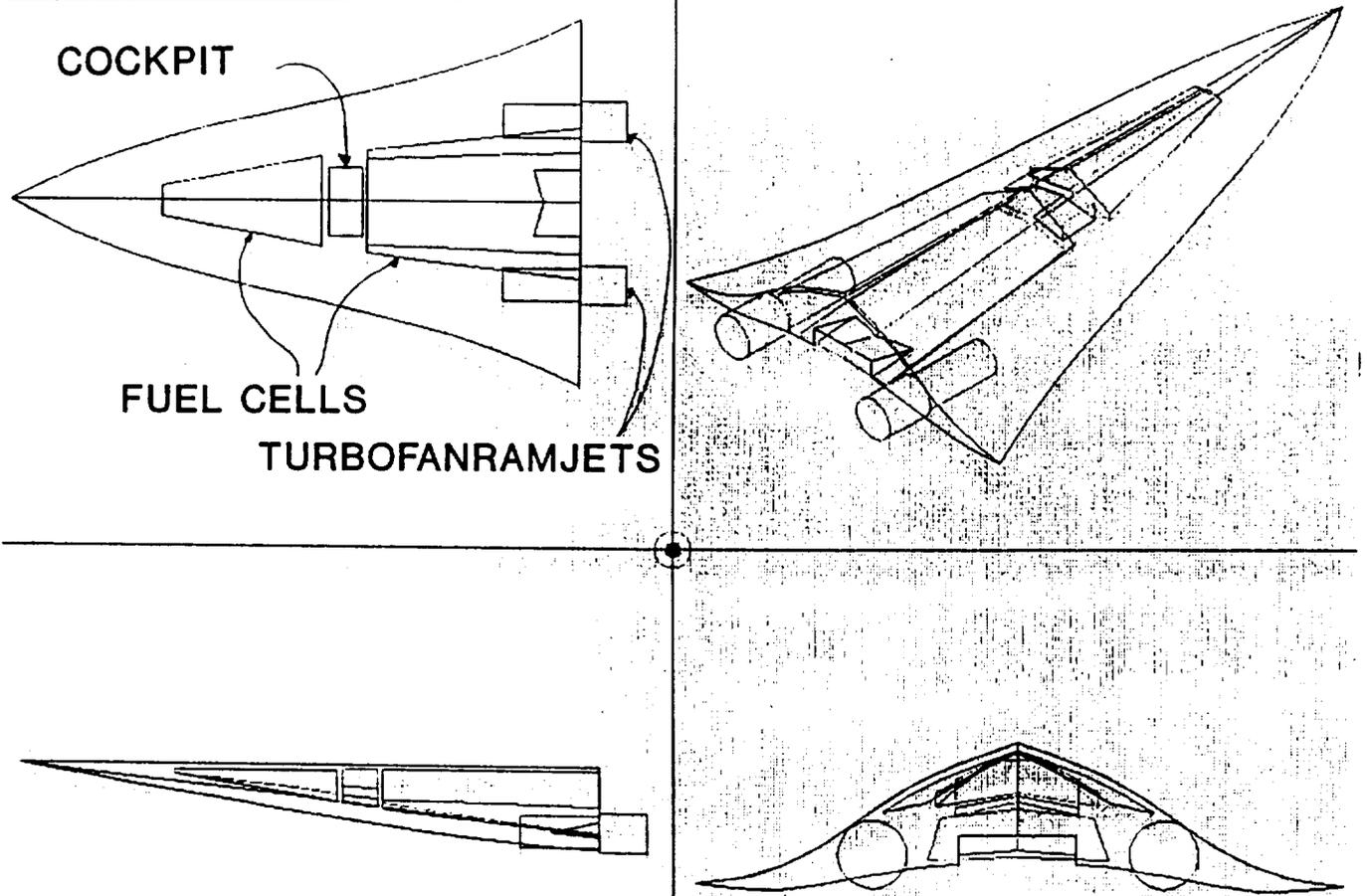
TURBOFANRAMJETS

After deciding to move the turbofan-ramjets away from the centerline of the aircraft, the question arose as to whether to make them protrude from the top or the bottom. At first, the choice was protrusion from the top. This maintained the idea of integrating inlet doors for the engines into the bottom of the aircraft. Later, it became apparent that this sort of inlet would be very complicated. Therefore, the idea of allowing the engines to protrude from the bottom of the aircraft became more feasible. This arrangement would allow room for a ramp inlet which would most likely result in a simpler system. The TFR engines were also moved rearward to further optimize their

internalization.

Another change made to the original MAXWARP waverider was the addition of a boat tail to the trailing edge of the wings. This boat tail differs slightly from that of the SCRAMjet section. The reason for the addition was to minimize base drag. Details on the geometry of these sections are available in the aerodynamics section of this report. The details of the configuration along with some of the design specifications can be seen in Figure 3.4 and Table 3.1.

HYPERSONIC WAVERIDER CONFIGURATION

Three-View Drawing
Red Group
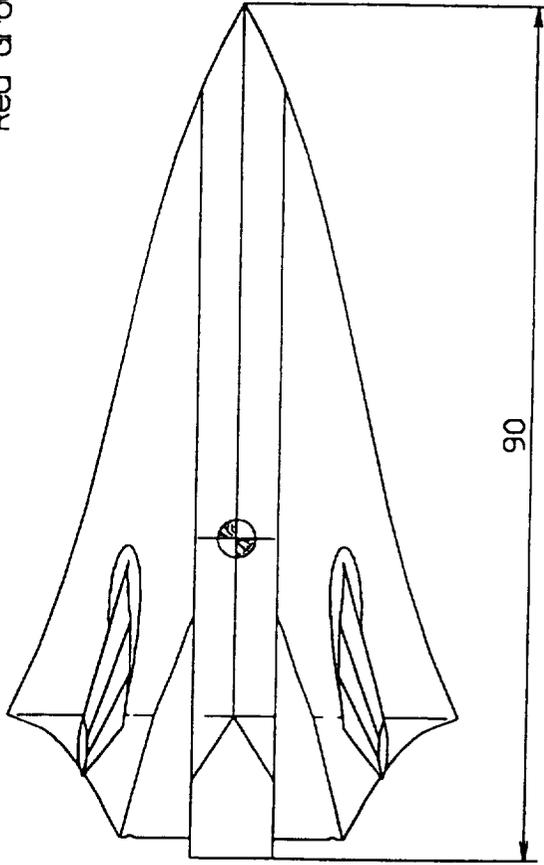
Critical Specs

T.O. Weight = 59,000 lbs.
Landing Weight = 47,500 lbs.
Engines: 4 G.E. Scramjet Modules
         2 G.E. Turbofanramjets

Fuel Volume: 2600 cubic ft.
L.E. Radius = 0.5 in.
Nose Radius = .5 ft.

47.9

90

11
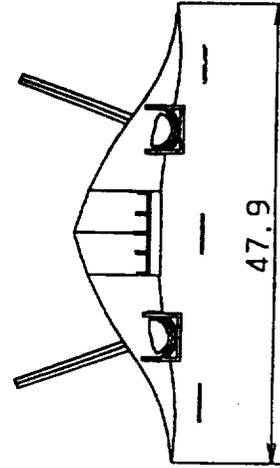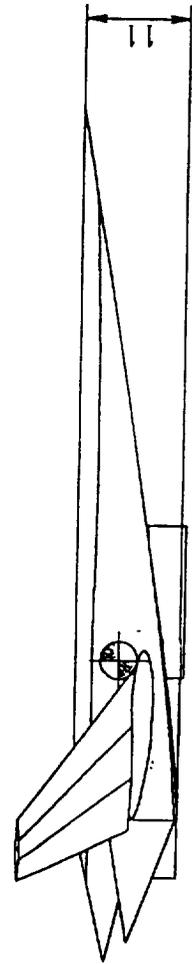
Table 3.1: Aircraft Specifications

Reference Area	2300	ft^2
Wetted Area	5100	ft^2
Aspect Ratio	1.0	
Takeoff Weight	59,000	lbs
Landing Weight	47,500	lbs
Fuel Weight	11,500	lbs
Fuel Volume	2,600	lbs
X_{CG} Empty	55.2	ft
X_{CG} Full	56.4	ft
X_{CP}	60.0	ft

3.3 Electrical Power Systems:

One important subsystem for this aircraft is the electrical power system. This system is responsible for supplying power to the life support, avionics, cooling systems, engine systems, and hydraulic systems. An engine starting system will most likely not be needed, however, since the engines can be windmilled for a start. The generation source must be very reliable and durable since this aircraft will be unable to fly without a means of control. A backup system will also be needed in case of main power failure. The biggest concern in choosing a power system is in minimizing the bulk of the apparatus. The amount of power that will have to be generated is unknown due to the lack of data on power requirements of advanced engine and control systems.

A promising candidate for the primary power system is that of a generator run by an air turbine. This method is very straightforward and reliable. Unfortunately, it also results in a sizable amount of drag due to the large quantity of air that must be used to turn the turbine. Another disadvantage is that the turbine would require a complex inlet system similar to that

of the turbofan-ramjets because of the large variations in speed during the flight.

A similar system to that above is the gas turbine system. This is basically a small turbojet used to power a generator. This method requires less air, but also requires fuel. An inlet system is also still required.

The most promising method of power generation is that of using fuel cells such as those used on the space shuttle. Fuel cells have an advantage in that they are enclosed systems. They have very few moving parts and are therefore less prone to mechanical failure. They are also have a high energy output in comparison to their size. The biggest question is that of whether the capacity of a reasonably sized fuel cell(s) is enough to power an aircraft of this size.

As is standard on most aircraft, a battery system will most likely be used as a secondary system. Nickel-cadmium batteries have been greatly improved in recent years, and would be a good choice for this aircraft due to their reliability and excellent performance.

3.4 Weight Analysis:

The weight analysis was the starting place in the design loop. For an initial estimate of the fuel requirements, it was assumed that 25% of the total weight of the aircraft at drop would be fuel. The total weight of the aircraft was divided into five primary systems: fuel, structural, thermal protection

systems (TPS), internal systems, and engine systems (see Table 3.2 for final weight breakdown). The weight iteration scheme was started by guessing a total weight. The amount of fuel that would be required to fly the entire mission was then calculated. A six percent burn off of the liquid hydrogen was included for the duration of the flight, and landing reserves were also included. The thrust required to overcome the drag at Mach 1 determined the size of the engines, and thus the weight of the engines. Data for the TFR engines was provided along with necessary sizing parameters. It was determined that two TFR engines scaled to 65% would be needed to provide the thrust.

Table 3.2: Weight Breakdown

Component	Weight (lbs)
Engine systems	19000
Fuel	11500
Internal systems	11000
Structural systems	12500
TPS	5000
Total Weight	59000 pounds

The SCRAMjet engine module weight, provided by General Electric, was stated to be 1300 pounds excluding inlet weight. A weight of 1000 pounds was assumed for the inlet of each engine cell. The total SCRAMjet engine weight was 9200 pounds.

The internal systems weight was based on empirical data found in Reference 6. The internal systems weight included: fuel tanks and insulation, pumps and drain systems, fuel center of gravity systems, life support systems, avionics, flight instruments, electrical systems, and landing skids. The internal

system weight was calculated to be 11000 pounds.

The fuel system weight was a function of the fuel requirements for the entire mission. This includes the fuel necessary for acceleration and cruise, cooling after the engines are stopped, reserves for landing, and an account for boil off. These fuel weights are given in Table 3.3.

Table 3.3: Fuel Weight Breakdown

Fuel Use	Weight (lbs)	
TFR Engines	4400	
SCRAMjet Engines	4500	
Engine Off Cooling	1200	
Boil Off	900	
Landing	500	
Total Weight	11500	pounds

The structural weight was a percentage of the total aircraft weight. A NASA technical report (Reference 1) was released which stated that for a potential (all wing configuration) type aircraft, with integrated fuel tanks, the structural and thermal systems should be approximately 24% of the entire aircraft weight. This percentage was to be divided between the thermal and structural systems equally. The methods used to determine this number were based on the bending moment requirements for a Mach 10 aircraft.

The 24% weight distribution was deviated from slightly for the aircraft. The 12% allowance for the TPS was supposed to have included insulation for the cryogenic fuel, however, the insulation was included with the weight of the fuel tank and counted as part of the internal systems weight. The structural weight was increased to over 16% to include the weight of the two

vertical tails, the boat tail, and the heavy turbofan-ramjet inlet and duct system.

The design loop started with an educated guess as to what the total weight would end up being. The fuel weight was then calculated, the internal weight was found, the engine weight, and structural weight were then determined. Once the individual weights were found, they were added up and if they did not match the initial guess exactly, the loop was started over with a new total weight. This loop was continued until the initial guess weight matched the calculated weight of all the systems.

The center of gravity analysis was performed after the aircraft configuration was finalized. The weight of the components was known, and the relative positions inside the aircraft structure was determined. By simply summing the moments about the leading edge of each of the components, and dividing by the total weight, the center of gravity location was determined. This was done for the aircraft under fully loaded and empty conditions; see Table 3.4 for CG location data.

Table 3.4: CG Location Analysis

Component	Weight (lb)	Position (ft)	Moment (ft-lb)
Body	11,256	50	562,800
TFR Engines	9,800	73	715,400
SCRAMjet	9,200	60	552,000
Vertical Tail	1,800	67	120,600
Fuel Tank 1	2,875	27	77,625
Fuel Tank 2	13,877	64	888,128
Avionics	2,352	45	105,840
TPS Top	1,000	41	41,000
TPS Bottom	4,000	43	172,000
Hydraulics	1,100	73	80,300
Boat Tail	1,740	80	139,200
	59,000		3,454,893

X_{CG} = 56.4 ft   (Full)
X_{CG} = 55.2 ft   (Empty)

3.5 Cockpit:

The cockpit is the central pilot system for this aircraft. To design the cockpit the Air Force Systems Command design handbook Crew Stations and Passenger Accommodations. The book was used as a guide to determine what systems would be required for the cockpit. The following is a list of these requirements:

1) Flight Controls

2) Landing Gear Controls

3) Emergency Controls

4) Powerplant Controls

5) Electrical Controls

6) Radio and Radar Controls

7) Miscellaneous Controls

After determining what systems were required, the cockpit was laid out. The cockpit for a typical side by side fighter was

used as a model, and shrunk for a single pilot. The final design

layout is presented in Figure 3.5.

Figure 3.5: Cockpit Layout

STATUS BOARD

FIRE EXTINGUISHING CONTROLS AND WARNING INDICATORS

STANDBY FLIGHT CONTROLS

FUEL THRUST RPM INDICATORS FOR TURBOFANRAMJET

FUEL THRUST INDICATORS FOR SCRAMJET

MASTER CAUTION PANEL

WARNING LIGHTS

FUEL MANAGEMENT DISPLAY

PROCEDURE CHARTS

OXYGEN

FUEL

TRIM

LIGHTING

ELECTRICAL

RADAR NAVIGATION

AUTO LAND CONTROLS

COOLING, PRESSURIZATION AND DEICING CONTROLS

AUTOPILOT CONTROLS

MAP STORAGE

CONTROL STICK

GLOBAL POSITION SCOPE

HORIZON INDICATOR

RATE OF CLIMB, AND ALTITUDE CONTROLS

ATTITUDE

AOA, MACH#, AND AIRSPEED

HEADING

LANDING CONTROL

SCRAMJET SHUTDOWN

TURBOFANRAMJET IGNITION

AFTERBURNER CONTROL

EXTERNAL VISION

TURBOFANRAMJET POWER

TURBOFANRAMJET SHUTDOWN

SCRAMJET IGNITION

SCRAMJET POWER

LANDING FLAP AND DRAG CHUTE CONTROLS

CRITICAL VOICE COMMUNICATION AND RADAR CONTROLS

DATA ACQUISITION CONTROLS

ELECTRICAL POWER, CIRCUIT BREAKERS AND LIGHT CONTROLS

19

Due to excessive heating on the forebody of the aircraft a conventional canopy could not be used. The pilot is totally enclosed in the aircraft and is in effect flying blind. Therefore it was necessary to provide the pilot with a Mechanical Optical System. This system is to be used for landing the aircraft. It consist of all optics, no electronics. This was done to ensure vision upon landing in the event of an electrical failure.

Finally, the ejection system was considered. The AFSC Design Handbook Crew Stations and Passenger Accommodations lists four types of ejection systems. Each has an altitude and speed constraint, and they are as follows:

1) Ejection Seats --- Altitude 50,000 ft
                      Speed 600 knots

2) Encapsulated seats --- Altitude 50,000 ft
                         Speed 700 knots

3) Encapsulated Pod --- Altitude above 50,000 ft
                       Speed above 700 knots

4) Nose Capsule --- Altitude above 50,000 ft
                   Speed above 700 knots

The biggest driver for the choice of the ejection system was not the altitude or speed constraints, but the weight constraint of the overall design. Due to the 75,000 lb limit on the aircraft it was decided to use the encapsulated pod. This configuration would provide adequate safety, while limiting the weight requirement for the system.

Overall, the provision of a pilot in this type of vehicle will help ensure the completion of the mission, as well as

provide extended research capabilities.

3.6 Landing Skids:

To eliminate unnecessary cooling, landing skids were chosen for the rear landing gear. A double wheel was placed in front to allow for steering capability. Since the cockpit would have to be cooled, the wheel was placed as close to the cockpit as possible (see Figure 3.6). The landing skids also eliminate bulky landing gear, since all available space would be filled with fuel tanks and structural support.

Figure 3.6: Rear Landing Skid

SHOCK ABSORBERS

2.65'

1.10'

0.75" 2.00'
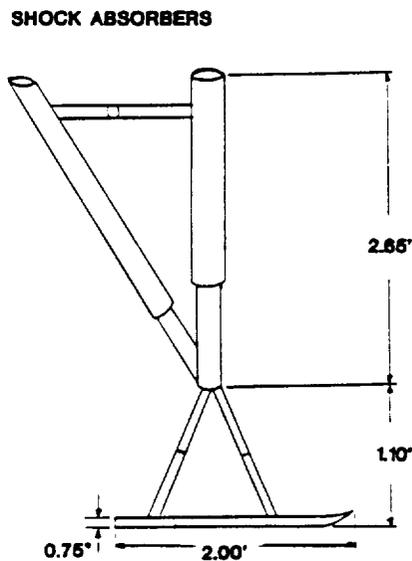
Should any problems occur that the aircraft would need to make an emergency landing, a drag chute would be used to help slow the aircraft at landing.

3.7 Configuration Modeling:

The MAXWARP program provided the necessary three-dimensional

21

coordinates of the struts, the leading edge of the aircraft, the nose, and the base of the waverider configuration. A program was written that uploaded the geometry points from the MAXWARP output into CATIA, a solid modelling software package. These geometric points were then connected in a smooth three-dimensional curve, and the leading edge and the base waverider configuration were therefore defined. In order to ensure the integrity of the overall configuration, the entire aircraft was developed utilizing solid modelling. The decision to design the aircraft utilizing solid modelling gives the designer several distinct advantages:

1.   The configuration could be developed to conform totally with the output of MAXWARP, which would justify high L/D values at hypersonic speeds.

2.   The internal systems, including the engine systems, could be modelled to scale, moved and placed in an optimized position, which would allow for maximum fuel volume and maximum ducting area.

3.   Solid modelling simplifies the process of developing a complicated geometry (i.e. the boat tail and the waverider configuration).

4.   Solid modeling ensures accuracy in sizing of all internal and external systems including measurement of internal volumes.

5.   Solid modeling ensures the accuracy of the three-view drawing and also presents a simplified problem of

obtaining these views since all hidden lines are
already removed.

6. Solid modeling ensures that everything does fit within
   the configuration and within desired specifications.

7. Industry is moving toward developing aerodynamic
   configurations in solid modelling so as to ensure the
   precision of all phases of design.

The basic principal in developing the waverider model was to
develop both the internal and external components of the plane as
separate solids. These separate entities include: the actual
waverider configuration, the TFRs, the SCRAMjets, the vertical
stabilizers, the cockpit, and the fuel tanks. By making each one
of these components a separate solid, the internal and external
systems could be positioned to optimize fuel volume and to ensure
that everything actually fit inside of the configuration. The
solid modelling also provided quick and accurate measurements of
the internal fuel volume. This alone justifies the usefulness of
solid modelling and guarantees accuracy in developing the overall
structure of the waverider.

Section 4: Mission Profile Analysis

Imperative to the design of an aircraft is a mission profile analysis. This analysis is required for sizing the overall aircraft as well as defining the individual systems and optimizing their performance. To accomplish this, an energy state program (PROFILE) was written. This program combines the aerodynamic characteristics, engine performance, and a flight path to compute the overall values of altitude, Mach number, and fuel usage. In addition, values such as the thrust used, dynamic pressure, and distance covered can be computed. This particular mission analysis program was written to minimize the fuel usage. The program works by computing the difference in flight conditions in small time steps. At each step, the thrust required for a minimum acceleration is computed. Using this thrust, the fuel usage and energy gain (kinetic and potential) is computed. After the minimum thrust calculation, higher thrust levels are tried. The thrust level that provides the maximum energy gain per mass of fuel is the one that is chosen for that time step. The program then continues to step through the flight of the airplane by achieving different points in the flight profile which are given as the input. Compiling the results from several runs of the program, the detailed characteristics of the flight profile can be analyzed and improved. With the program, changes in aircraft weight, engine scale, and L/D profiles can also be made easily and new results obtained quickly.

While the PROFILE program did optimize the thrust level for minimum fuel usage, it was necessary to control the input to insure that the flight parameters were favorable for all aircraft operations. The flight path had to be one that took full advantage of the operational ranges of the engines. The dynamic pressure also had to be maintained within the range where it was possible to cool the aircraft.

By interactively using the PROFILE program the detailed flight profile was determined. Initially, the results were concerned with the overall evaluation of the mission. These runs provided information needed for the rough sizing of the aircraft as well as estimates of fuel usage and range for different possible configurations. As the configuration of the aircraft became better defined, the PROFILE program was again used to optimize individual system performance. An example was the addition of a fourth SCRAMjet module. While three modules provided adequate thrust for the mission, the use of a fourth allowed the individual modules to operate at a more efficient lower level of thrust. In this instance the savings in fuel weight was equal to the weight of that module. Therefore, the gross takeoff weight remained the same while the fuel usage decreased substantially. Since fuel space was one of the critical factors in completing the mission, this was of great benefit.

Results from PROFILE also identified a critical aspect of the mission. This was the acceleration through Mach 1. At this

point the thrust was about equal to the drag. The thrust pinch is evident in the plot of thrust and drag versus Mach number (shown in Figure 4.1). A small solid rocket was considered to overcome this obstacle. It was found that a 3000 pound rocket was adequate. Another solution was to dive the aircraft through Mach 1. Using a 5000 foot dive, the aircraft was able to get through Mach 1. However, the fuel usage increased by 750 pounds. Although the extra weight could be tolerated, the use of a dive was favored over the rocket to avoid the complexity of an additional propulsion system.

Figure 4.1:   Thrust and Drag vs Mach Number
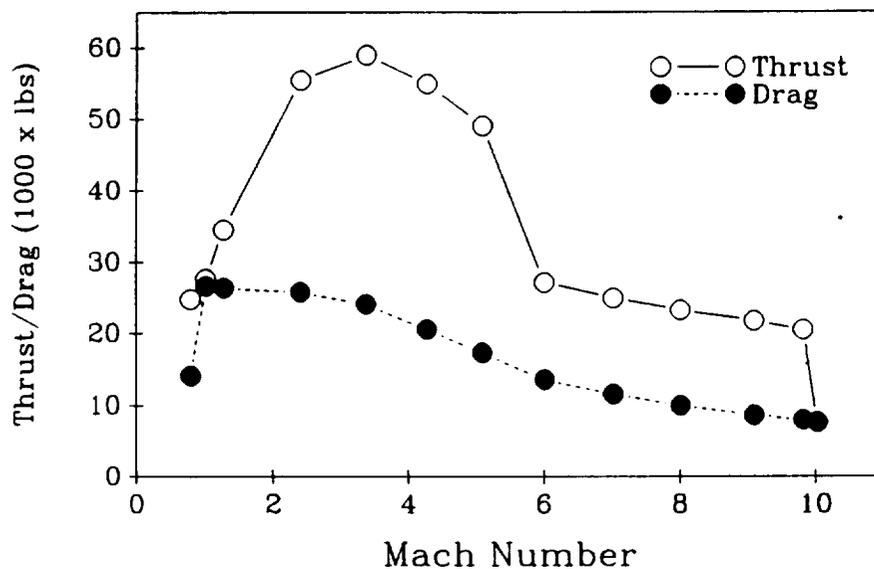
When all of the factors such as propulsion and dynamic pressure were considered, the flight profile shown in Figures 4.2 through 4.4 was arrived at. The dive through Mach 1 is apparent in all three of the figures. Figure 4.2 demonstrates the large distances covered by such an aircraft. The upper limit of dynamic pressure of 2000 psf can be seen in Figures 4.3 and 4.4.

Figure 4.2: Flight Distance Profile

Figure 4.2: Flight Distance Profile

Labels in figure: SCRAM; M = 10, t = 16 min; M = 6, t = 5 min; M = 10, t = 14 min; Coast; Transition; TFR; M = 0.8, t = 0 min; M = 1, t = 35 min; M = 0.6, t = 42 min. Altitude (1000 x ft); Distance (miles)
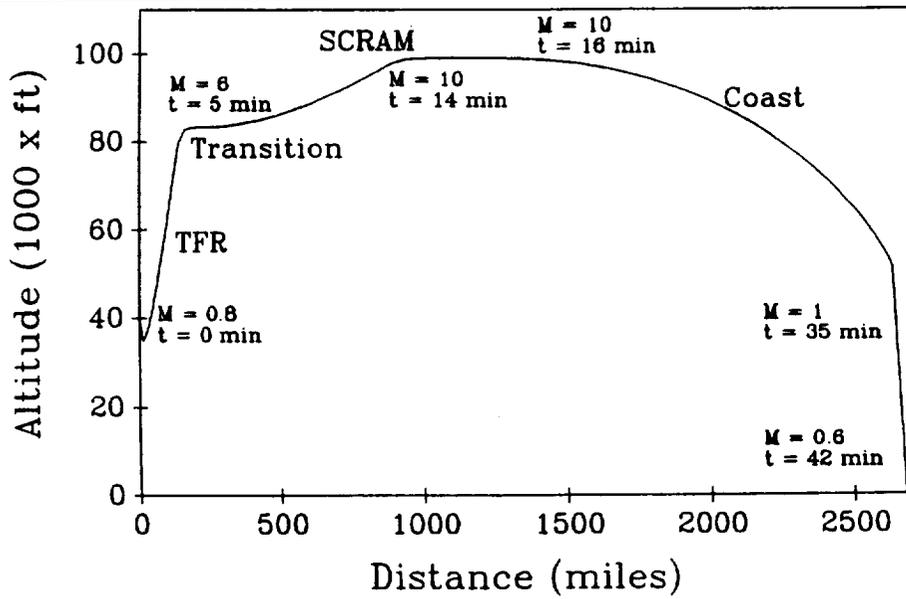
Figure 4.3: Flight Mach Number Profile (Ascent)

Figure 4.3: Flight Mach Number Profile (Ascent)

Labels in figure: Transition; TFR; SCRAM; Q = 1000; Q = 1500; Q = 2000. Altitude (1000 x ft); Mach Number
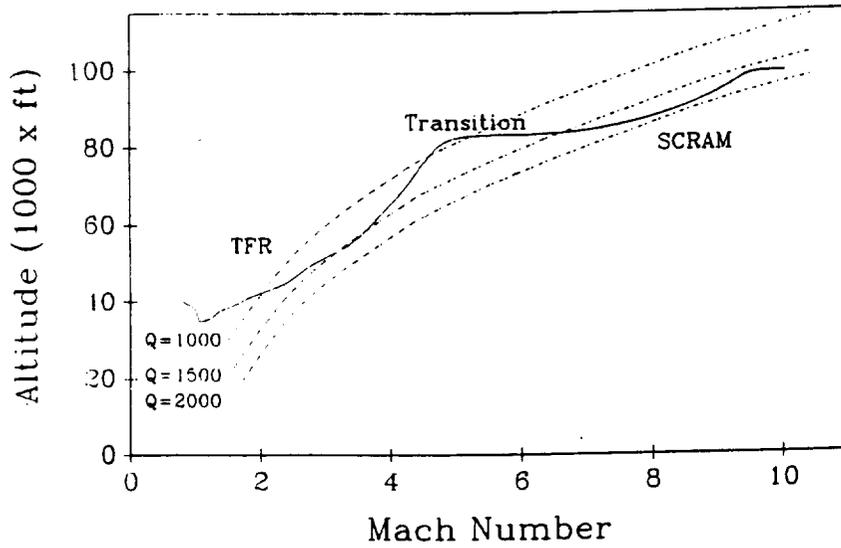
Figure 4.4: Flight Mach Number Profile (Descent)
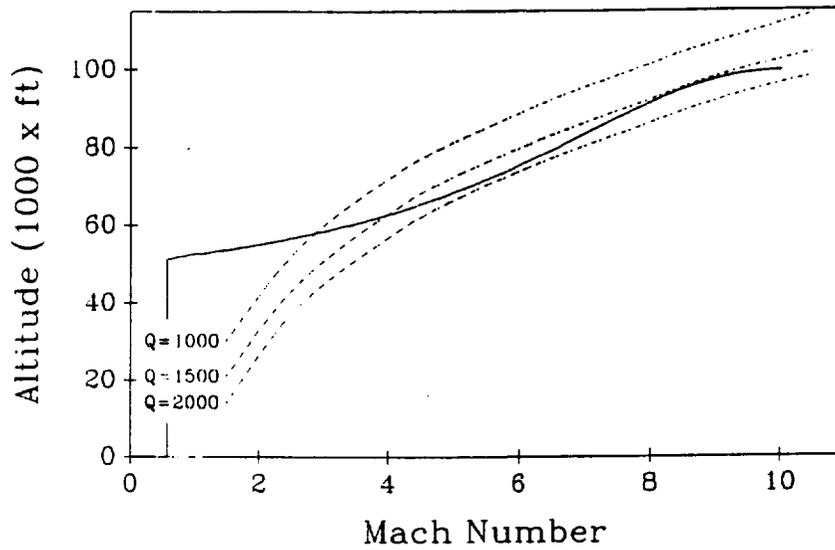
A final consideration of the mission analysis is where the
flight of the aircraft will actually take place. The sonic
overpressures (see Figure 4.5) created by the shock waves from
the aircraft are typically between 1.0 and 0.5 psf. These
overpressures are generally within the FAA limit on aircraft
noise which is set at 1.0 psf. However, the sudden and
unexpected nature of the noise created by a sonic boom makes it
less acceptable for the same levels. Therefore an over water
flight path (shown in Figure 4.6) was chosen to limit the
disturbance caused by the overpressures. The nominal 200 mile
distance from the coast reduces the level of the sonic
overpressure heard on land by one quarter. Although no part of
the supersonic flight takes place over land, it is necessary to
decelerate through Mach 1 near the coast on the way to the Dryden
Flight Test Center. This is required to insure that the aircraft
has sufficient energy to glide to a landing if the TFR engines

fail to restart. This will cause a stronger overpressure in one small area along the coast, but will not exceed the FAA limitations.

Figure 4.5: Sonic Overpressures
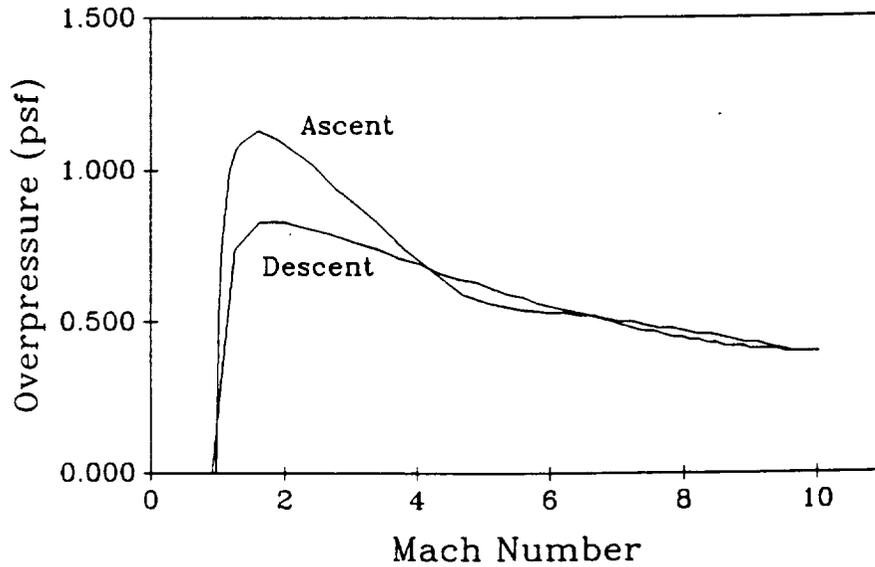
Figure 4.6: Flight Path
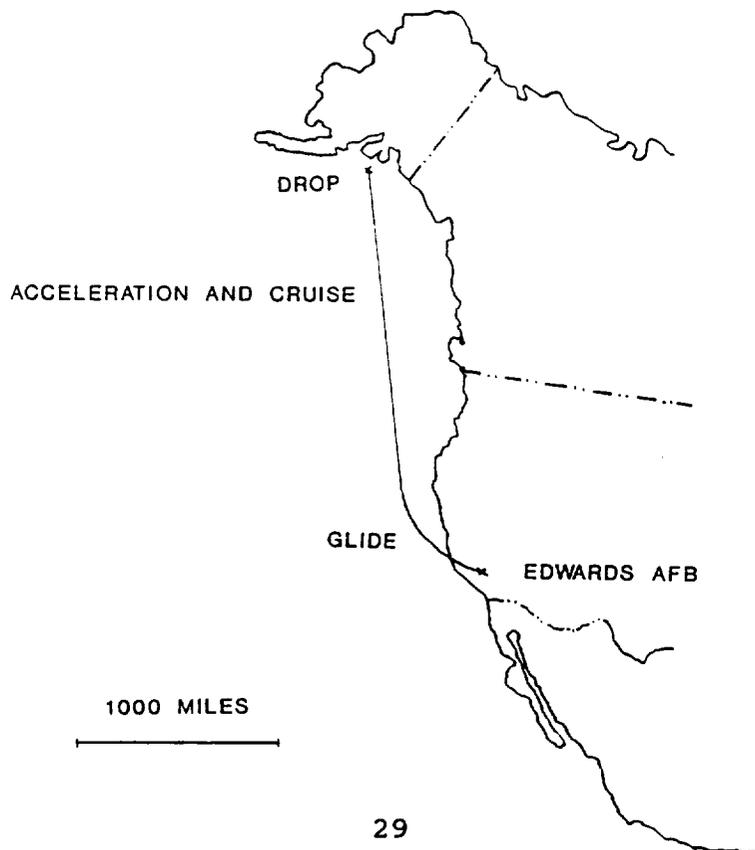
Section 5: Aerodynamics

5.1 Subsonic Aerodynamics:

Three methods were used to estimate the subsonic lift and drag on the waverider configuration. The first two methods were derived from empirical equations. The third was the use of a wind tunnel test. The first method was for a low aspect ratio delta wing with an elliptical cross section. The method was based on empirical data and proved to be inaccurate when compared to the other two methods. The second method was given in the text by Leland Nicolai. The theory presented was for small aspect ratio wings with sharp leading edges and accounted for non-linear effects. The results of the second method are presented in Figure 5.1 along with the supersonic and hypersonic results. This figure contains the data that was used for the fuel usage calculations.

Figure 5.1: Drag Polar (Theoretical)
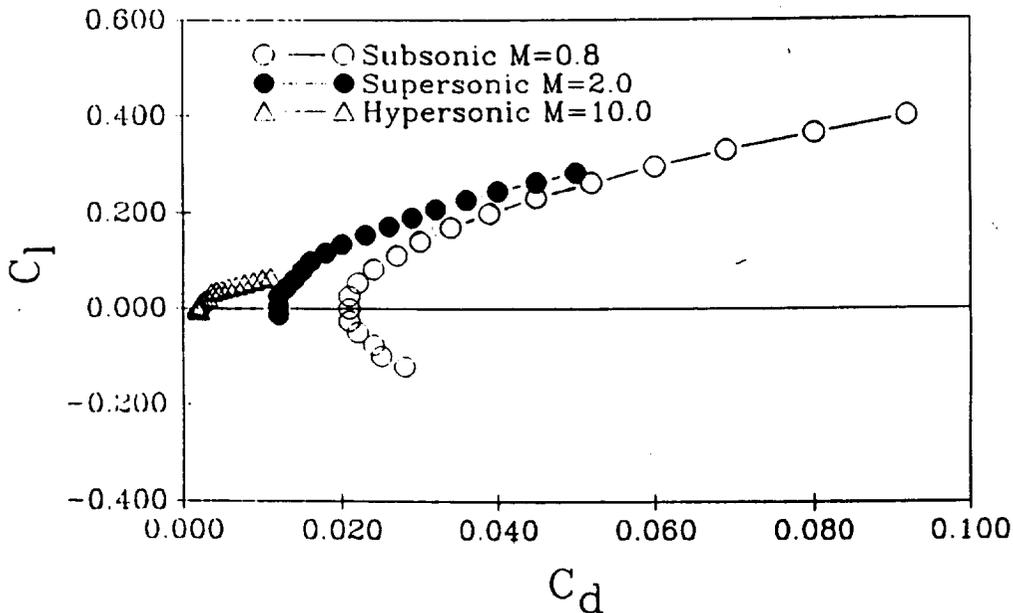
The data from the wind tunnel experiments (see Appendix A) is shown in Figures 5.2 through 5.5. As can be seen, the lift data agrees very well up to an angle of attack of approximately 10 degrees. Above ten degrees, the experimental data becomes non-linear. There are a number of possible explanations for the behavior of the model at this point. It is thought that, due to the low Reynold's number at which the test was run, the flow over the model is most likely all laminar. Therefore, a stall will occur much easier at lower angles of attack than might occur on a full sized aircraft of this shape. Such a stall may have occurred on the wing tips where the local Reynold's number is extremely low. This can be seen as the small loss of lift shown on the graph. This transition can be seen to occur sooner for the higher velocity. Why this occurs is unknown. Where the entire body stalls is unknown due to limitations on the balance. The final stall angle is expected to be very high due to the delta shape of this aircraft.

Figure 5.2:   Lift Coefficient vs Angle of Attack
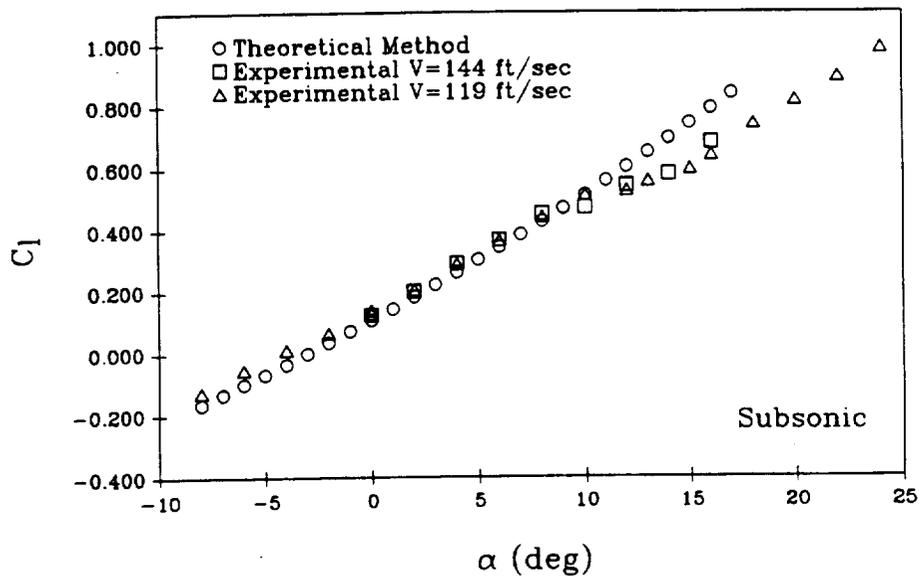
Figure 5.3:   Drag Coefficient vs Angle of Attack
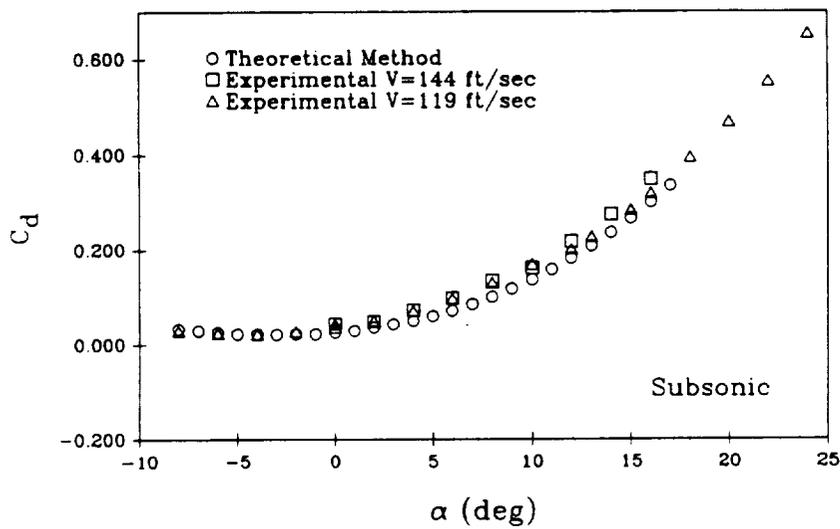
Figure 5.4: Moment Coefficient vs Angle of Attack
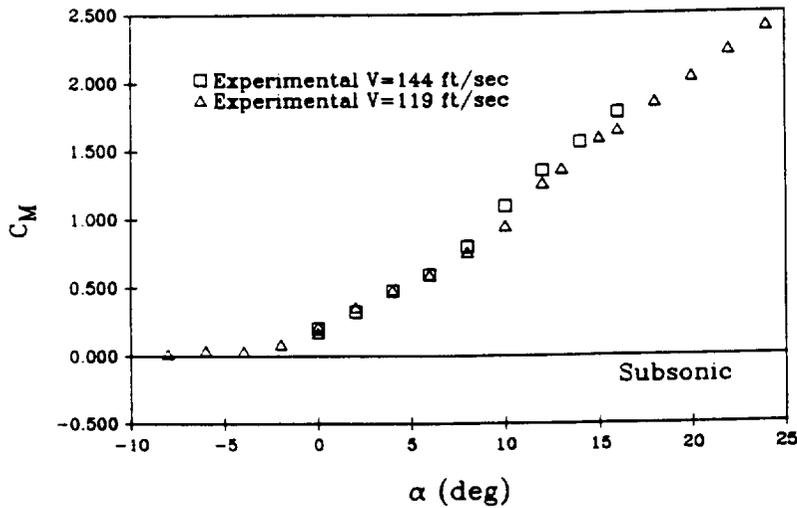
Figure 5.5: Drag Polar (Experimental)
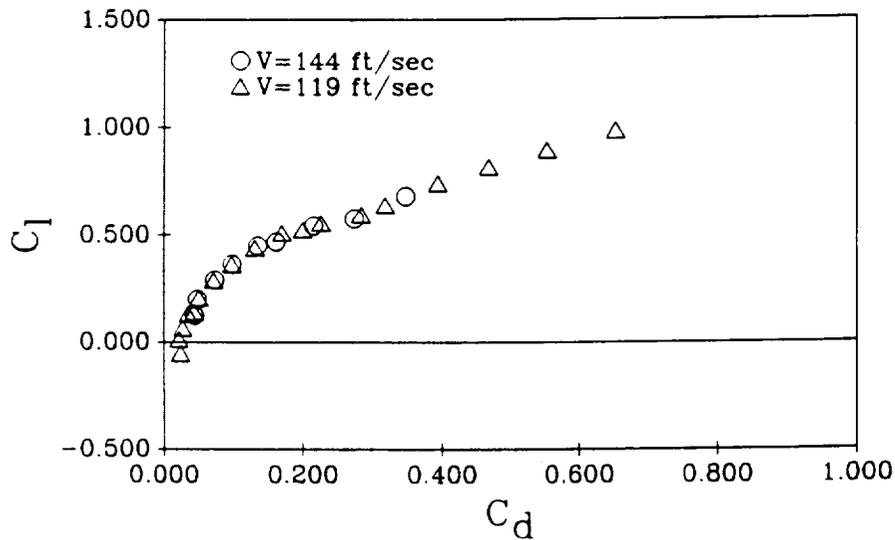
The drag coefficients can be seen to match very well with the theoretical data. The drag coefficients from the experimental data are slightly higher due to the addition of the engine nacelles on the model.

In addition to the unusual stall characteristics of this model, there were a number of other interesting observations made during the testing. During the slower run, the model began to

vibrate at an angle of attack of fifteen degrees. It was thought that the aircraft was about to stall, but the data showed that the model was still following a basically linear lift curve. This was thought to possibly be a Reynold's number effect, or a harmonic generated by the wind tunnel itself.

One notable problem with this design is the large pitching moment generated. The values can be seen in Figure 5.4 for the moment coefficient about the center of gravity. A stability augmentation system will be needed to deal with this problem.

5.2 Transonic Region:

In the transonic region, normal shocks form on the airfoil which induces separation. This in turn increases the drag and decreases the lift. The theory used for calculating subsonic and supersonic coefficients does not attempt to predict these values in the transonic region, approximately M=0.8 to 1.2. For this reason the values between the subsonic and supersonic values are fared-in to approximate the transonic region.

5.3 Supersonic and Hypersonic Aerodynamics:

One important parameter in the determination of the aircraft performance is an accurate determination of the lift and drag at speeds above Mach 1. This importance is evident when one considers that most of the flight occurs at these speeds.

Two different methods were used to calculate the supersonic lift and drag. One method was taken from the text by Leland

Nicolai and was based on supersonic linear flow theory corrected for three-dimensional flow effects.

The wing lift curve slope is a function of Mach number, wing aspect ratio, and taper ratio. The top surface of the aircraft was again taken as the zero reference line.

The supersonic drag was broken into two parts: friction drag, and wave drag. The skin friction was based on the wing wetted area, the reference area, and the skin friction coefficient. The skin friction coefficient was based on the cutoff number and flight Reynold's number.

The wave drag was based on a biconvex airfoil shape with sharp leading edges. The method used was based on experimental data combined with empirical methods.

The other method used to obtain the lift and drag on the aircraft utilized shock-expansion theory. Allowances were made for real gas effects above Mach 5. The reason shock-expansion theory was chosen was because of the unique geometry of the waverider body. The basic waverider shape has the same geometry at every longitudinal cross section, allowing the oblique shock formed at supersonic speeds to remain attached to the leading edge.

One addition to the waverider body was a boat tail at the trailing edge and at the exhaust ramp of the SCRAMjets in order to reduce the base drag. Above Mach 6, the use of the SCRAMjet causes the boat tail to be a thrust surface rather than a drag surface. Allowances were made for this in the shock expansion

35

program.

Due to structural limitations and engine constraints, the cross sectional airfoil geometries of the aircraft could not be made the same at all locations. Therefore, the aircraft was split into several sections. A program was written to perform the shock expansion calculations and is outlined in Appendix B. This program found the pressure distribution on each of the four faces of an airfoil cross section for a given angle of attack, free stream static pressure, and Mach number using oblique shock and Prandtl-Meyer expansion relations. The pressures were then translated into axial and normal forces using the corresponding area and geometry of each face. The axial and normal forces were then translated into lift and drag by relating the normal and axial forces to the angle of attack.

The program allowed the user to input the desired Mach number and free stream static pressure corresponding to the altitudes obtained from the flight path previously calculated. The program then used these constants to calculate the lift and drag for several angles of attack at a variety of Mach numbers and altitudes, so that the lift-to-drag ratios for the flight path could be calculated and output. The resulting drag polar is shown in Figure 5.1. The lift to drag ratios were found by sorting through the data obtained until the angle of attack was found at which lift equaled weight (lift is nearly equal to weight at all points of the flight path). The final lift to drag ratios for the flight path can be seen in Figure 5.6.

Figure 5.6: Lift to Drag Ratio vs Mach Number
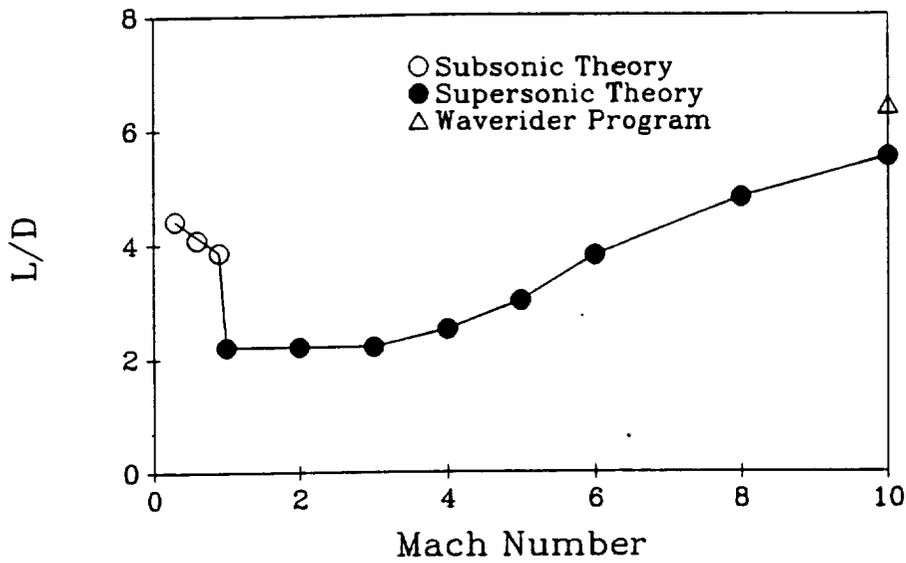
An approximation was made for the contribution of friction drag. Friction drag is less of a factor at hypersonic velocities because of the tremendously high Reynold's number. However, at supersonic speeds, it is still a considerable fraction of the drag.

Using the results from the program, the boat tail geometry was optimized to provide the best lift to drag ratios through the flight range. Due to constraints placed on the boat tail by the SCRAMjet exhaust ramp and size of the fuel tanks, certain parts of the boat tail could not be changed much. However, satisfactory results were obtained using this procedure.

A few interesting characteristics were noted from the data. Very small (.2 degree) changes in angle of attack resulted in very significant changes in lift produced. The drag, however, did not change significantly. These characteristics can be attributed to the large lifting area of this aircraft. This will

place significant demands on the stability control system.

Another method was used for estimating the hypersonic lift and drag. Newtonian flow theory was used as a check against the shock expansion theory. The waverider was modeled as a two dimensional wedge. The results obtained were very similar to those from the shock expansion theory.

5.4 Stability:

A detailed stability analysis was performed for the aircraft. Longitudinal and lateral stability derivatives were calculated for flight Mach numbers of 0.8, 5.0, and the design speed of Mach 10.0. These derivatives are shown in Tables 5.1 and 5.2.

Table 5.1: Longitudinal Derivatives

	M=0.8	M=5.0	M=10.0
C_{DU}	-0.0222	-0.0003	-0.0001
C_{LU}	-0.1552	-0.0148	-0.0071
$C_{D\alpha}$	0.0727	0.0285	0.0140
C_{DO}	0.0125	0.0018	0.0036
C_{LO}	0.0873	0.0356	0.0136
$C_{L\alpha}$	1.5390	0.8160	0.7800
C_{MU}	0.9367	0.0626	0.0348
$C_{M\alpha}$	-0.0934	-0.0575	-0.0637
X_U	-0.0139	-0.0016	-0.0017
X_W	0.0043	0.0035	-0.0009
Z_U	-0.0972	-0.0054	-0.0050
Z_W	-0.4574	-0.3978	-0.1882
M_U	-0.0297	0.0076	0.0019
M_W	-0.0076	-0.0069	-0.0035
M_q	0.0000	0.0000	0.0000
M_{Wdot}	0.0000	0.0000	0.0000

Table 5.2: Lateral Motion Derivatives

	M=0.8	M=5.0	M=10.0
$C_{y\beta}$	-0.3412	-0.1205	-0.1152
$C_{l\beta}$	-0.0002	-0.0002	-0.0002
$C_{n\beta}$	0.1019	0.0147	0.0139
C_{yp}	0.2509	0.0252	0.0254
C_{lp}	-0.1282	-0.0680	-0.0650
C_{np}	-0.0171	-0.0017	-0.0017
C_{yr}	0.0000	0.0000	0.0000
C_{lr}	0.0342	0.0034	0.0034
C_{nr}	-0.1005	-0.0378	0.0383
$C_{y\delta a}$	0.0000	0.0000	0.0000
$C_{l\delta a}$	0.0017	0.0011	0.0018
$C_{n\delta a}$	-0.0001	-0.0001	0.0000
$C_{l\delta r}$	0.0387	0.0153	0.0130
$C_{n\delta r}$	0.0587	0.0214	0.0210
Y_{β}	-0.1006	-0.0652	-0.0276
L_{β}	-0.0197	-0.1834	-0.1684
N_{β}	4.2277	24.4236	19.8093
Y_{p}	1.7753	0.2942	0.1464
L_{p}	-0.3989	-0.3151	-0.1383
N_{p}	-0.0213	-0.0032	-0.0014
Y_{r}	0.0000	0.0000	0.0000
L_{r}	0.1064	0.0158	0.0072
N_{r}	-0.1251	-0.0701	-0.0326
$L_{\delta a}$	0.1867	0.9267	0.8153
$N_{\delta a}$	-0.0041	-0.0085	0.0000
$Y_{\delta r}$	0.0000	0.0000	0.0000
$L_{\delta r}$	4.2733	5.1741	5.9378
$N_{\delta r}$	-3.7713	-11.6996	-5.6010

The longitudinal analysis included all stability derivatives required for the 4 X 4 matrix analysis used in the state variable representation (see Tables 5.3 and 5.4). Values for the coefficients of the moment about the center of gravity for a tailless aircraft were included. This value include effects in the moment due to inlet forces. The change in moment due to alpha was also calculated. This coefficient is one of several stability coefficients that convey the inherent natural stability of the aircraft. The requirement that this value be negative is met for all flight conditions. Generally for a tailless aircraft, the static longitudinal stability is unstable. The wing is usually destabilizing and needs the tail to balance the moment forces. In this case the aerodynamic center of the large lifting surface is aft of the center of gravity, which gives us a positive static margin and thus a stable configuration.

Table 5.3:   Longitudinal Eigenvalues M=0.8

$$
\begin{bmatrix}
s + 0.0139 & -0.0043 & 0.0000 & 32.200 \\
0.0972 & s + 0.4574 & -800.00 & 0.0000 \\
0.0297 & 0.0076 & s & 0.0000 \\
0.0000 & 0.0000 & -1.0000 & s
\end{bmatrix}
$$

Characteristic Equation:

$$s^4 + 0.4713(s^3) + 6.0868(s^2) - 0.7696(s) - 0.4136 = 0.0$$

Table 5.4: Lateral Eigenvalues M=0.8

$$\begin{bmatrix} s + 0.1006 & -0.0022 & 1.0000 & -0.9598 \\ 0.0197 & s + 0.3989 & -0.1064 & 0.0000 \\ -4.2277 & 0.0213 & s + 0.0701 & 0.0000 \\ 0.0000 & -1.0000 & 0.0000 & s \end{bmatrix}$$

Characteristic Equation:

$$s^4 + 0.5696(s^3) + 4.3051(s^2) + 1.6708(s) - 0.4304 = 0.0$$

The lateral analysis was performed in a similar manner. All required stability derivatives were calculated that were needed for the state variable matrix analysis. The three lateral stability modes were considered.

The dutch roll mode was checked and found to be stable. The spiral mode was also calculated, but found to be unstable. This particular mode is extremely slow and the FAA allows for this mode to be unstable. The roll rates were calculated and compared to other aircraft.

It needs to be pointed out that all modes, with the exception of the spiral mode are stable at all flight speeds. It also needs to be pointed out that the natural damping in all cases is poor. The low damping leads to poor flight quality and is completely unacceptable, thus a stability augmentation system will be needed. The poor damping is the result of the tailless aircraft having no tail to provide the lift to oppose any sudden changes in angle of attack. There is also no pitch damping provided for a tailless aircraft. The only damping is dependant on the static margin which in this case is small because the a.c is very close to the center of gravity. The lateral damping

41

characteristics are poor because the all wing configuration does allow not stabilization due to relative flow around the fuselage. The dihedral effect associated with wings at an angle is beneficial for roll stability only when the dihedral angle is positive, or upward. The anhedral angle for the aircraft is destabilizing.

A cross wind analysis case for landing was performed and used to determine the required rudder size. The cross wind case was only required during landing but was performed at the three mentioned flight speeds. As expected all rudder deflections were acceptable.

An asymmetric power condition was also done at all Mach numbers and their respective thrust values. The rudder size required for the cross wind case had no problems meeting the asymmetric power condition requirements.

The elevons and ailerons were never actually sized to meet any climb or roll conditions. The moderate angles of attack and lack of any maneuvering requirements for an experimental aircraft of this nature allowed the aircraft control surfaces to be somewhat flexible.

As stated before, the inherent poor flight quality caused by the low natural damping will necessitate the use of a stability augmentation system. By the estimated flight date, it is believed that the state of the art in feed back control systems will be a fly-by-light augmentation system. This will greatly reduce weight and complexity from todays electronic systems.

The short term approximations were calculated for all three mentioned flight speeds (see Tables 5.5 and 5.6). Comparisons were made for the Mach 0.8 case between the approximations and the eigenvalue solutions of the state variable matrix. All values showed excellent agreement.

Table 5.5: Longitudinal Approximations

	M=0.8	M=5.0	M=10.0
Freq. (rad/sec)	2.47	5.87	5.92
Damping Ratio	0.097	0.034	0.016
Period (sec)	2.60	1.07	1.06
$t_{1/2}$	2.90	3.47	7.34
$N_{1/2}$	1.13	3.24	6.93

Table 5.6: Lateral Approximations

	M=0.8	M=5.0	M=10.0
I (1/sec)	2.50	3.14	7.23

Dutch Roll Mode	M=0.8
Freq. (rad/sec)	2.06
Damping Ratio	0.0548
Period (sec)	3.06
$t_{1/2}$	6.12
$N_{1/2}$	2.00

5.5 Landing Analysis:

The landing speed was determined by using a Cl_{max} = 1.0. The stall speed for the all wing configuration of the waverider, 148 feet/second, is relatively low because of the large wing area. Touchdown speed was $1.15V_{stall}$, or 170 ft/s. The ground roll for the landing was based on the friction coefficient of the skids for a hard dirt landing strip. This distance was 3,975 feet. This length can be considerably lowered using a drag chute and some form of airbrakes.

Section 6:   Propulsion

6.1   Engine Selection:

This aircraft has three powered flight required phases: launch and acceleration to SCRAMjet operating conditions, acceleration and cruise using SCRAMjet engines, and powered landing. Initially, the use of a rocket booster was considered to reach SCRAMjet operating conditions. It was found that the large mass of propellant required would make it difficult for the aircraft to remain under the design weight limit of 75,000 pounds. In addition, the use of a rocket booster would not allow the possibility of a powered landing without an additional propulsion system. The General Electric turbofan-ramjet (TFR) engine, shown in Figure 6.1, can be used during the acceleration to SCRAMjet transition, and also restarted to provide go-around capability for landing. It was chosen for these reasons. Two fuels, methane and hydrogen, are available to power the TFR engines. Hydrogen has a high energy per unit mass, but its low density gives it a low energy per unit volume (Figure 6.2). The TFR engine powered by hydrogen thus has a significantly lower SFC than the one powered by methane, but the volume of fuel burned is much higher. Since the SCRAMjet engine operates only on hydrogen, it is advantageous to use hydrogen for the TFR to remove the need for two fuel systems. It was determined that the volume penalty of hydrogen could be tolerated, and it was the fuel chosen for the TFR as well as the SCRAMjet.

44

Figure 6.1: General Electric Turbofan-Ramjet
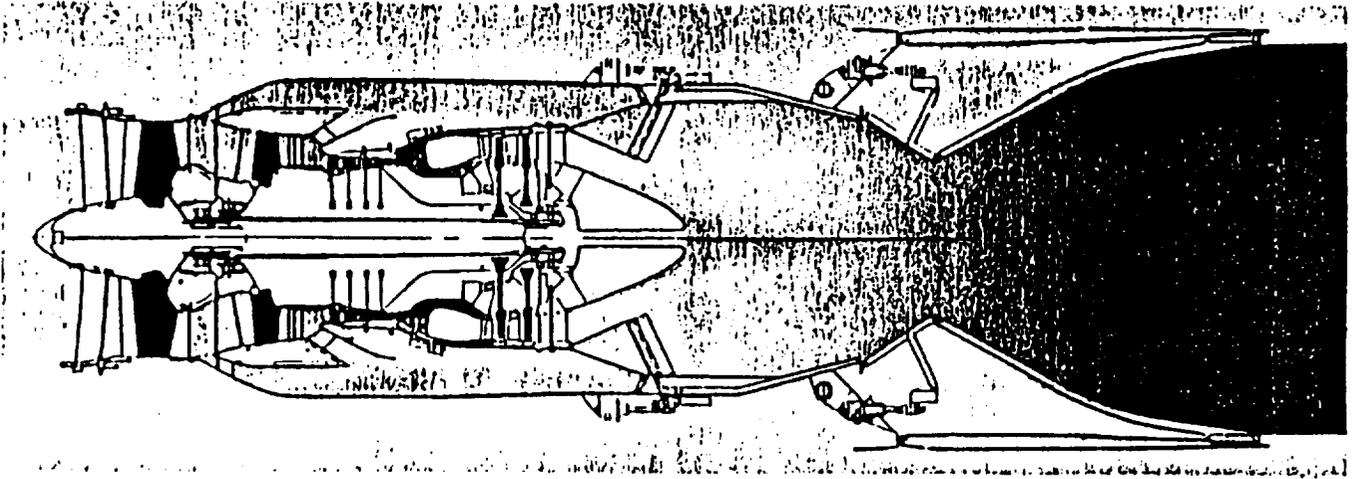
Figure 6.2: Fuel Comparison
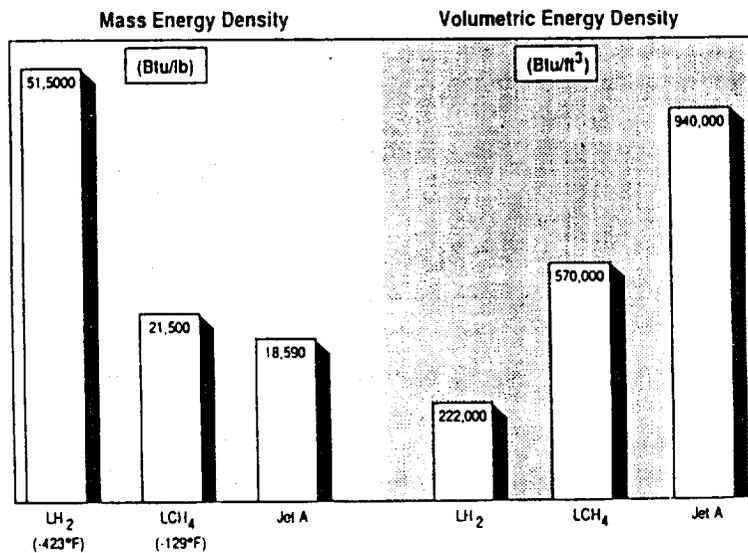
The thrust available at a given Mach number for the hydrogen fueled TFR engine is a strong function of altitude (Figure 6.3), making mission profile optimization important. The inlet will require variable geometry to provide the correct mass flow to the engine at every Mach number and to seal the engine at speeds above Mach 6.

45

Figure 6.3: Turbofan-Ramjet Engine Performance
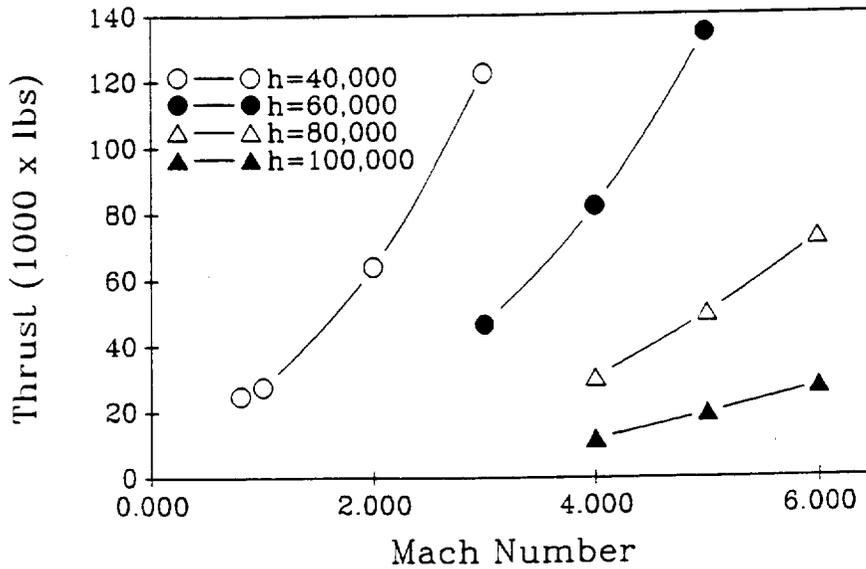
The General Electric SCRAMjet engine module is shown in Figure 6.4. Because the individual engines provide low thrust levels, several modules must be used. The fuel weight for the operation of four modules at a low thrust level is much less than operation of three modules at a higher thrust level. This reduction in fuel weight is equal to the increase in the engine weight for the fourth SCRAMjet module. Four modules were chosen because the reduction in fuel weight (and volume) allows a reduction in the size of the aircraft. The SCRAMjet engines are very sensitive to the operating dynamic pressure, with thrust decreasing sharply with altitude gain for constant Mach number (Figure 6.5). These dynamic pressure considerations must be accounted for in the choice of a flight profile.

Figure 6.4: General Electric SCRAMjet Module
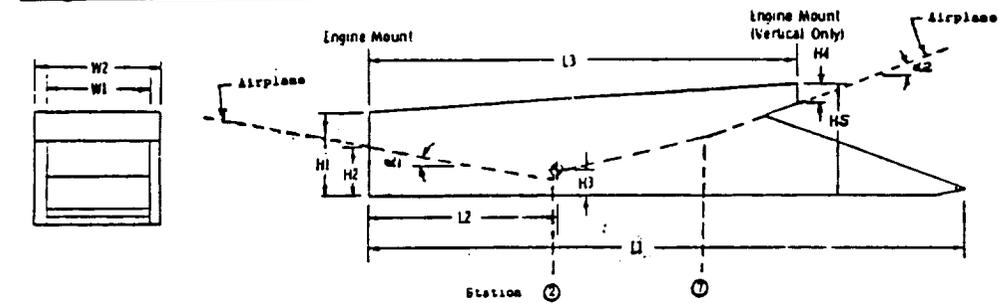
COMBUSTOR DESIGN

COMBUSTOR INLET, STATION ②, MACH
NO. IS BETWEEN 0.3 AND 0.5 OF
THE FREE STREAM MACH NO.

MODULE WEIGHT

BASE WEIGHT FOR 30 INCH FLOWPATH
WIDTH MODULE IS 1330 LB.

FOR FLOWPATH WIDTH OF 35 INCHES,
SAME BASE HEIGHT AND LENGTH,
SCALED MODULE WEIGHT IS 1580 LB.

FOR FLOWPATH WIDTH OF 20 INCHES,
SAME BASE HEIGHT AND LENGTH,
SCALED MODULE WEIGHT IS 920 LB.

BASE MODULE DIMENSIONS

L1	OVERALL MODULE LENGTH	160.6 INCHES
L2	LENGTH TO CG	47.6
L3	UPPER MODULE LENGTH	108.3
H1	FORWARD MODULE HEIGHT	21.5
H2	FLOWPATH FRONTAL HEIGHT	12.4
H3	HEIGHT TO CG	6 6
H4	AFT UPPER MODULE HEIGHT	4.0
H5	AFT TOTAL MODULE HEIGHT	27.0
W1	MODULE FLOWPATH WIDTH	30.0
W2	MODULE WIDTH *	W1 + 6.7
α1	INLET RAMP ANGLE	10 DEG.
α2	EXHAUST RAMP ANGLE	20 DEG.

* ADJACENT MODULES MAY SHARE ONE 6 IN. WALL

Figure 6.5: SCRAMjet Engine Performance
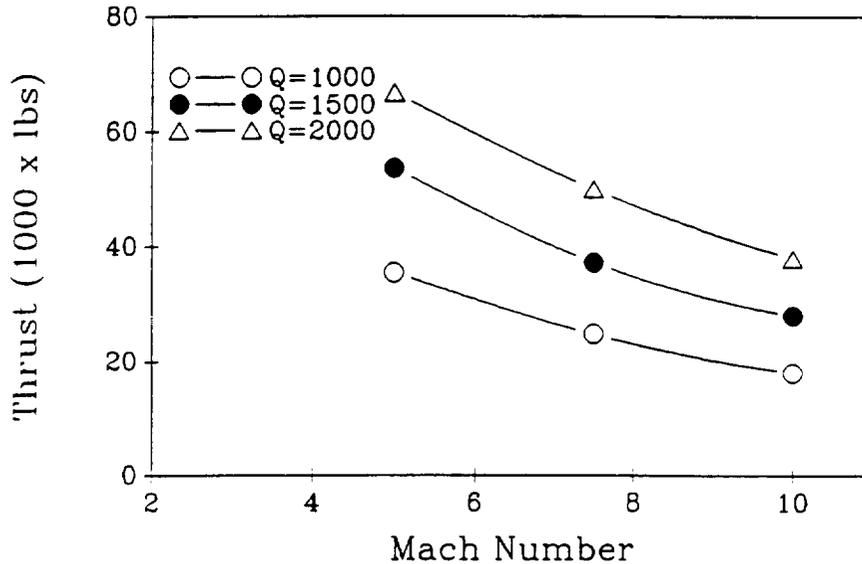
The SCRAMjet exhaust is expanded against the rear of the
airframe, providing additional thrust and lift. Thus, at high
Mach numbers when the engine is operating, the base drag from the
expansion ramp is reduced considerably. Below Mach 6, the

SCRAMjet will be sealed off, as the TFRs are, should this be advantageous for drag reduction or protection of data acquisition equipment.

6.2 Turbofan-Ramjet Inlets:

The capture area for each 65% scaled TFR engine varies from 21.5 square feet at Mach 0.8 to 4.0 square feet at Mach 6 and 80,000 feet. An 8.0 foot wide by 2.7 foot high inlet will deliver the proper mass flow at Mach 0.8 (see Figure 6.7). After the flow at 80,000 ft is slowed to subsonic, the flow area is 0.35 square feet. With an 8.0 foot wide inlet, however, the flow height is just 0.5 inches; Clearly boundary layer effects would choke the flow. Therefore, a split inlet system has been designed (see Figure 6.6). The inboard side of the inlet has a capture area of 4.0 square feet. The outboard side of the inlet accounts for the remaining 17.5 square feet of capture area. At Mach 0.8, both sides of the inlet are completely open and the engine will have the correct mass flow. At Mach 5, the outboard side is completely closed and no air enters (see Figure 6.9). The inboard side is open to the proper 4.0 square feet of capture area and the height at the throat is 2 inches. At the intermediate speed of Mach 2 and 52,000 feet the capture area required is 8.0 square feet. The Inboard side of the inlet is open to 4.0 square feet and the outboard side is opened the remaining 4.0 square feet (see Figure 6.8). In order to match the temperature and pressure for the subsonic flow of each side

48

of the inlet, the shocks must have the same strength, and thus the ramp angles are the same. Cowl, pressure, friction, and spillage drag for a side of the inlet are charged to the engine when the inlet delivers air to the engine and to the airframe when the inlet is sealed off.

Figure 6.6: Turbofan-Ramjet Inlet (Isometric View)
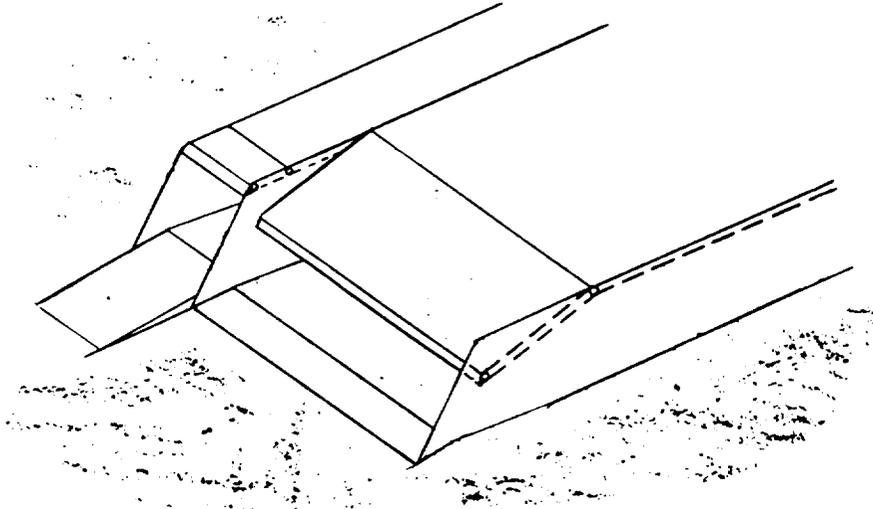
Figure 6.7: Turbofan-Ramjet Inlet M=0.8

FRONT VIEW   SIDE VIEW

OUTBOARD   INBOARD

37.8

18.0

96.0

32.3

95.7

AIRCRAFT
UNDERBODY

49
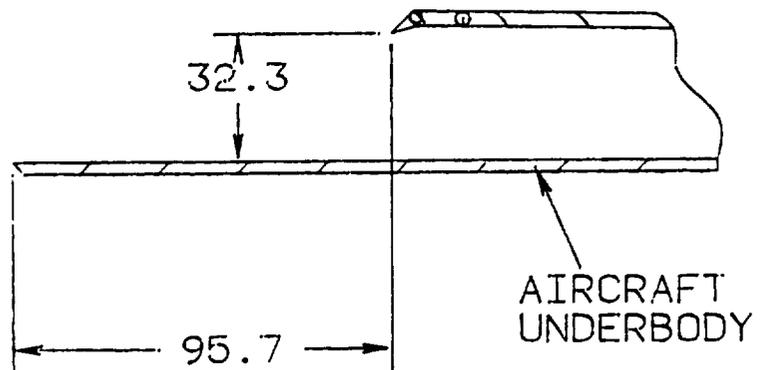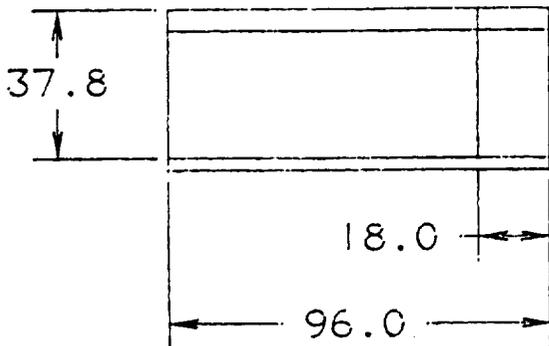
Figure 6.8: Turbofan-Ramjet Inlet M=2.0

OUTBOARD

AIRCRAFT
UNDERBODY

FRONT VIEW

SIDE VIEW

INBOARD

OUTBOARD

32.3

10.7

18.0

96.0

INBOARD

AIRCRAFT
UNDERBODY
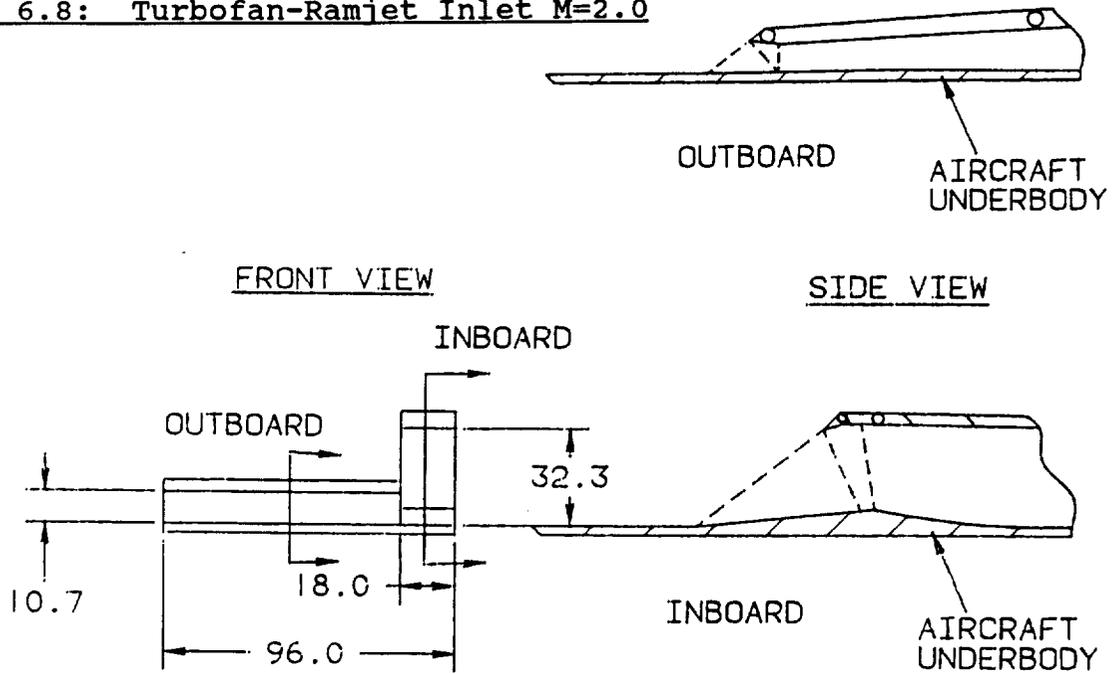
Figure 6.9: Turbofan-Ramjet Inlet M=5.0

FRONT VIEW

SIDE VIEW

INBOARD

OUTBOARD

INBOARD

32.3

8° 8′

11° 23′

18.0

9° 35′

96.0

95.7

AIRCRAFT
UNDERBODY
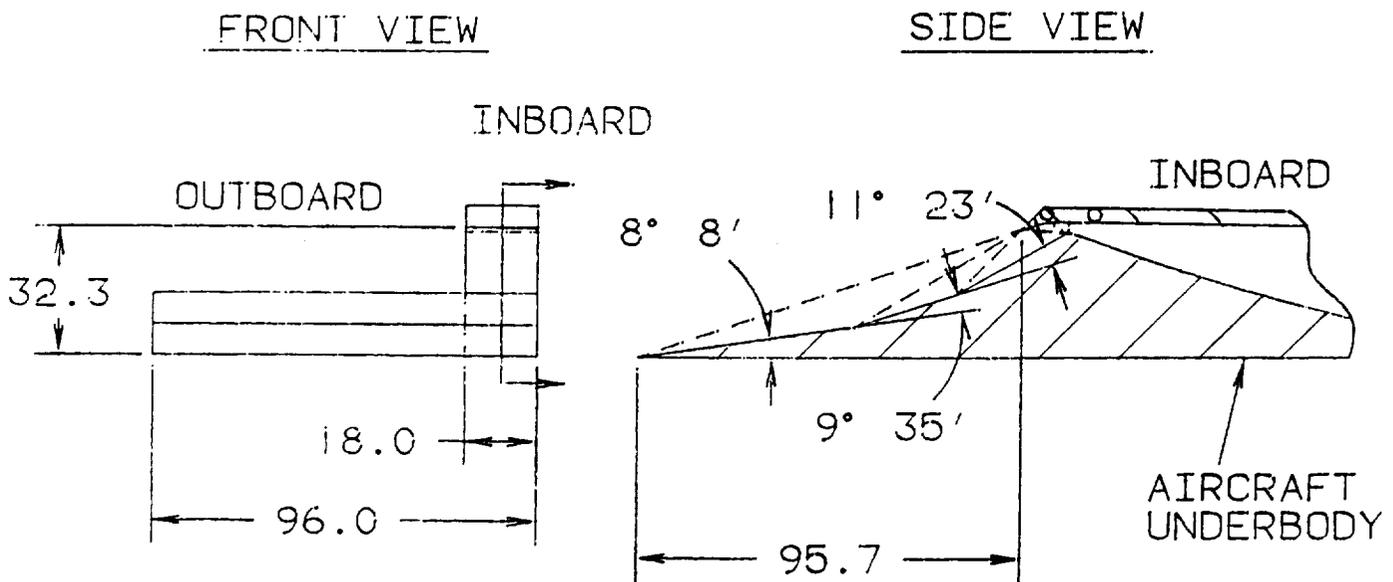
Though the inlet will provide the engine with the proper mass flow during the entire operating range, the inlet is designed to be matched at Mach 5. The external shocks are designed to impinge on the cowl lip eliminating spillage drag.

The pressure recovery is optimum when the shocks are all of the same strength. This occurs when the normal Mach number for all oblique and normal shocks is the same. If 5 oblique shocks and 1 normal shock are used with a pressure recovery of 65%, the 7th (number of shocks + 1) root of .65 gives the pressure recovery across each shock. The pressure recoveries for this inlet are shown in Figure 6.10. These recoveries are defined as the fan face pressure over the free stream pressure. The shock and flow turn angles, along with the state variables, are known through the entire inlet. For Mach 3 and 4, the inlets are not matched, and the spillage drag is accepted. The TFR engines are operating for such a short time that the additional fuel burned is much lighter than the heavy, complex inlet system necessary to match the inlet at all Mach numbers.

Figure 6.10:   Inlet Pressure Recovery
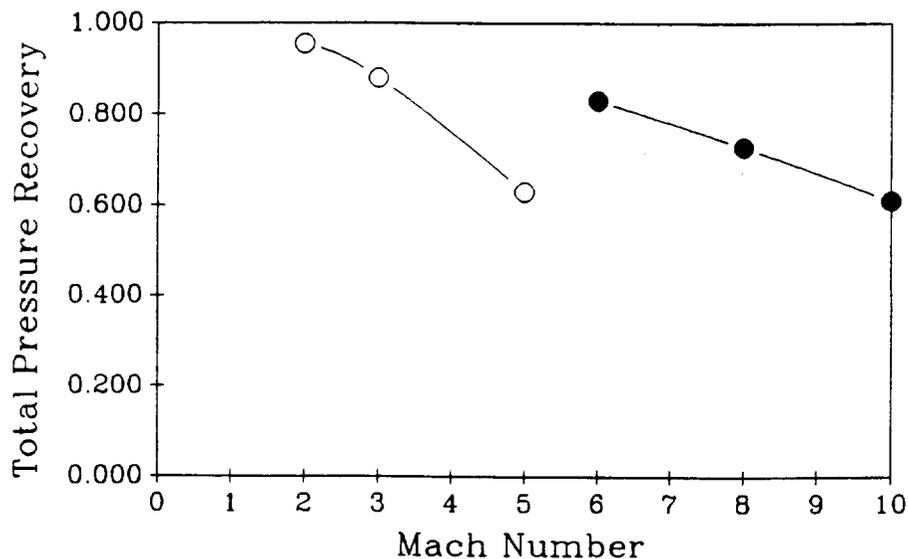
6.3   SCRAMjet Inlets:

The basic SCRAMjet module consists of an external compression

ramp and a flat plate parallel to the free stream forming a convergent channel. The inlets must have a capture area variation between 3.2 square feet at Mach 6 and 2.2 square feet at Mach 10. The modules are 2.5 feet wide so at Mach 6, a height of 15.2 inches is required at the cowl lip. An external ramp of 6.75 degrees was chosen to bring the total flow turn to 10.0 degrees plus any angle of attack, consistent with the General Electric engine description. The height at the entrance to the combustor is 3.1 inches with oblique shocks slowing the flow to 45% of free stream Mach number (Figure 6.11). The bottom plate is hinged, and for the Mach 10 case (see Figure 6.12) is turned up parallel to the external ramp. The ramp is placed such that the oblique shock impinges on the cowl lip at Mach 10. The combustor entrance height is also 3.1 inches at Mach 10. The pressure recoveries are shown in Figure 6.10. These recoveries are defined as the combustor inlet pressure over the free stream pressure.

Figure 6.11: SCRAMjet Inlet M=6.0

UNDERSIDE OF AIRCRAFT

WEDGE HALF ANGLE

3° 15'   6° 45'   RAMP SURFACE   3.1

15.2

42.9

HINGE

101.8
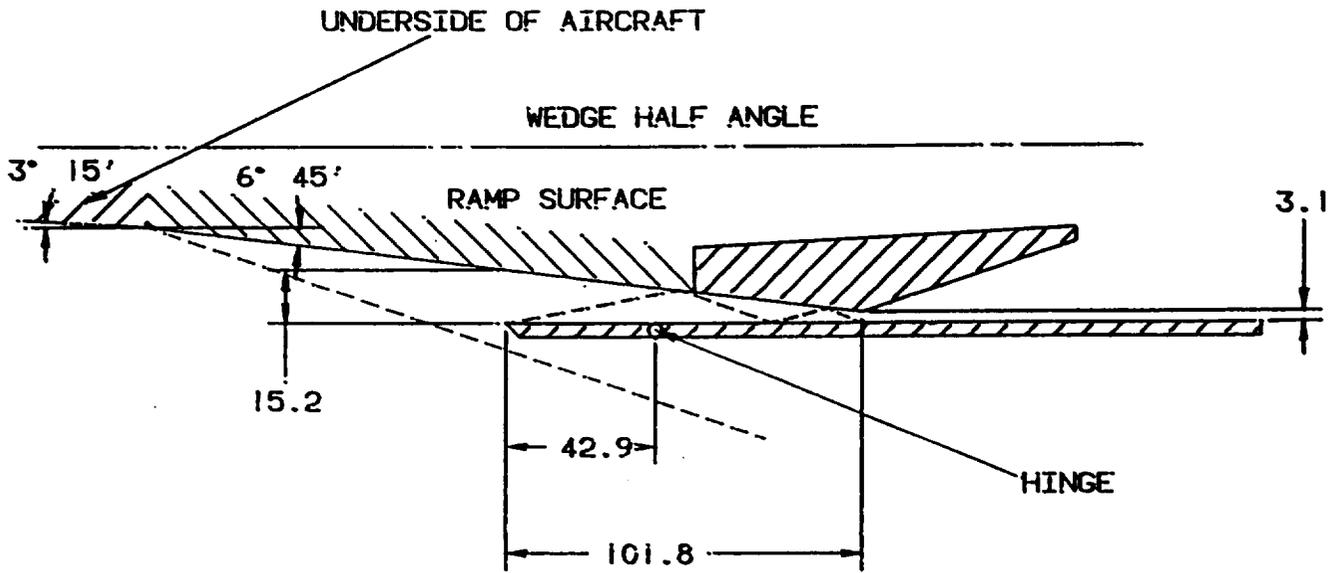
Figure 6.12: SCRAMjet Inlet M=10.0

UNDERSIDE OF AIRCRAFT

WEDGE HALF ANGLE

3° 15'   6° 45'   RAMP SURFACE   3.1

10.1

42.8

101.7   HINGE
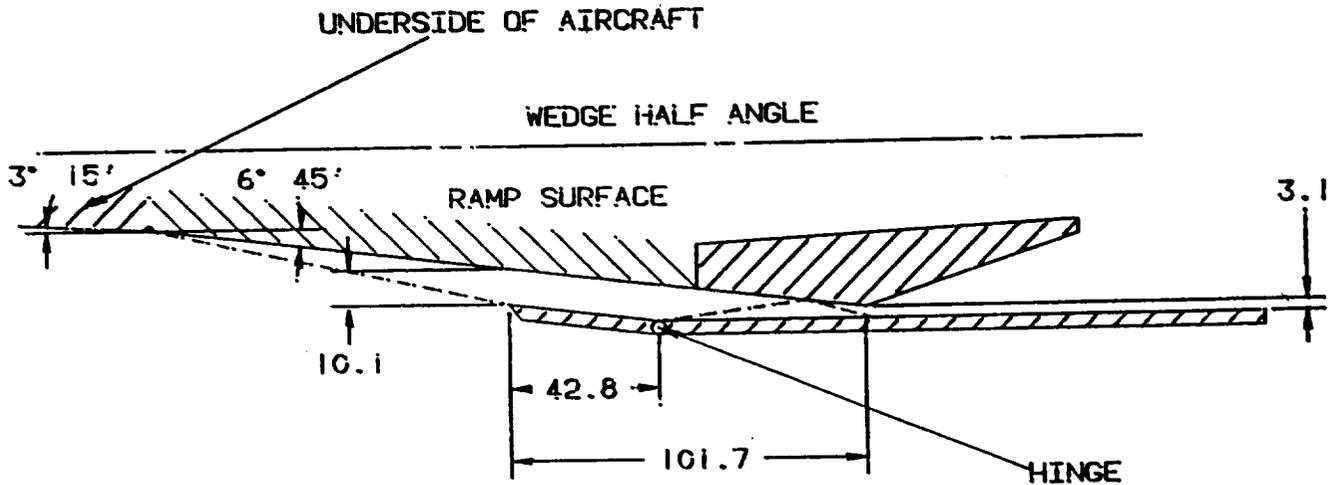
Between Mach 6 and 10, shock-shock interactions will occur.
A complete full rotational method-of-characteristics analysis
would be necessary to give a detailed calculation of the inlet
performance at these intermediate points. However, the mass flow

was calculated for these cases with the assumption of no
rotation.

6.4 SCRAMjet Diffuser:

An expansion nozzle for the SCRAMjet engine was created
using the method of characteristics for a minimum length nozzle.
The nozzle would have to fit a length of 23 feet and height of 7
feet in order to keep the aircraft the same size.

To expand the flow fully and turn the flow to be parallel to
the free stream would take more length and height in the
expansion nozzle than could be hoped for. This was expected
before the analysis began. For the given aircraft geometry, it
is not possible to fully expand the gas due to the lack of the
necessary area ratio. The best performance can then be obtained
by providing the maximum turning possible to bring the exit flow
parallel to the free stream. The unavoidable result is a deficit
in thrust compared to the provided engine data.

In the effort to create a nozzle to turn the flow parallel
to the free stream an interesting solution presented itself.
Instead of creating more turning in the exhaust nozzle, the
engine could be mounted at an upward angle. This angle could be
optimized to create a parallel flow at the exit. In addition,
the effective expansion height becomes greater (and thus the exit
area increases). Figure 6.13 demonstrates the flow angles and
effective expansion height for the case of the SCRAMjet mounted
parallel to the free stream and with it angled upward. Because

this solution would involve a redesign of the SCRAMjet inlet

there was not time to study it fully. This would, however, be an

interesting topic to evaluate.

Figure 6.13: SCRAMjet Diffuser Schematic

SCRAMjet mounted parallel.
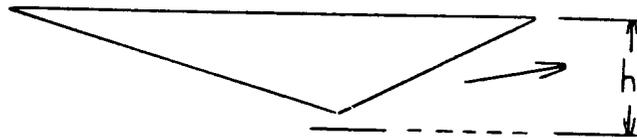
SCRAMjet mounted at an angle.
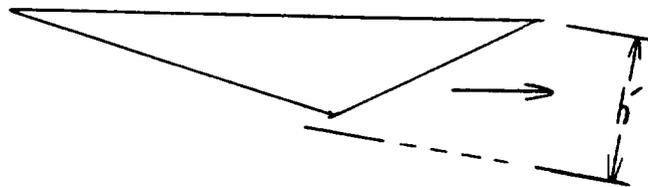
Section 7: Cooling

7.1 Cooling Requirements:

It was realized immediately that in order to specify and detail the complicated cooling systems, the actual temperatures that the aircraft would be experiencing must be determined. In order to determine the wall temperatures, a program was developed that determined the skin temperature distribution. The methodology used in developing the program is outlined in Appendix C.

Heat transfer coefficients were calculated assuming that all parts of the waverider were isolated bodies (i.e. the nose, the leading edges, the top surface, and the bottom surface). With this in mind, the effects of flow interference induced by the proximity of one body with another, including shock and boundary layer interactions, and viscous effects were not included. In all cases, both laminar and turbulent heat coefficients were determined using curve fitting techniques based on existing empirical data. Once the local Reynold's number exceeded 500,000, the flow was assumed completely turbulent. It must be noted that no attempt was made to model the transition from laminar to turbulent flow. The MAXWARP output gave us a transition from laminar to turbulent at 5.8 feet from the leading edge. The local Reynold's number of 500,000 showed good agreement with this number and transitioned at approximately 6.0 feet from the leading edge.

The skin temperature distribution for the upper and lower surfaces shown in Figures 7.1 and 7.2 were determined assuming the worst possible heating case for the aircraft. This case corresponds to a free stream Mach number of 10, the upper surface parallel to the free stream, and the lower surface at a 6.13 degree angle of attack relative to the free stream. This case also assumes that no shock wave is forming on the top surface of the aircraft, since it is parallel to the free stream, and would allow that surface to rapidly cool off. Real gas effects were accounted for by assuming frozen flow with a gamma of 1.3. A plot of the temperature distribution including all major vehicle components is shown in Figure 7.3.

Figure 7.1: Temperature Distribution (Top Surface)
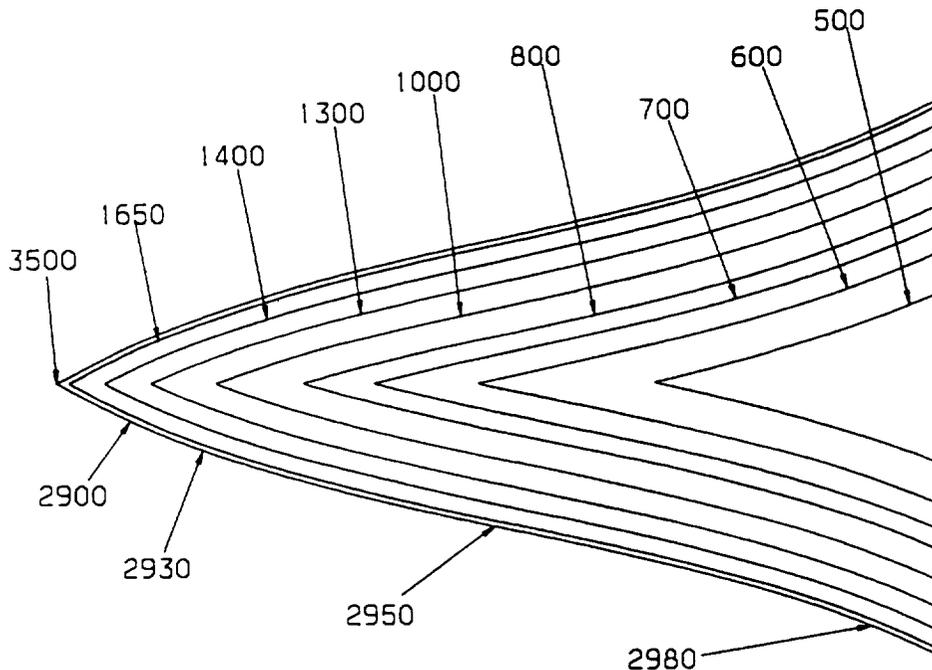
UPPER SURFACE
TEMPERATURE DISTRIBUTION
(Degrees Fahrenheit)

Figure 7.2: Temperature Distribution (Bottom Surface)

LOWER SURFACE
TEMPERATURE DISTRIBUTION
(Degrees Fahrenheit)

(Figure labels: 2000, 2200, 2600, 1800, 1600, 800, 1400, 1600, 3500, 1400, 1200, 1000, 900)
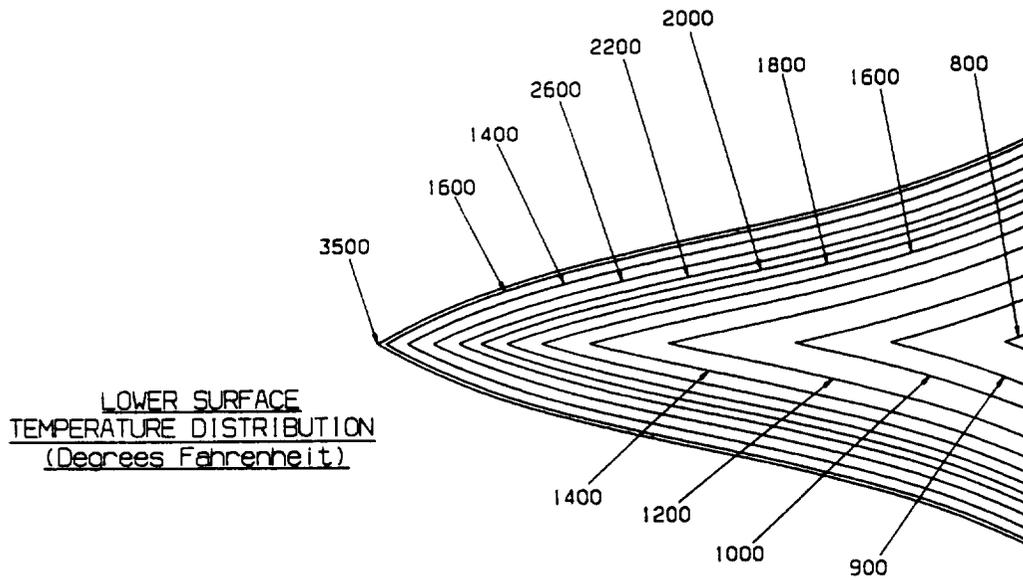
Figure 7.3: Temperature Distribution (Components)

(Figure labels: 1400, 1100, 1850, 2900, 3500, 1600, 1400, 2600, 2000, 2900, 3700, 1400)

TEMPERATURE DISTRIBUTION
VEHICLE COMPONENTS
(degrees Fahrenheit)
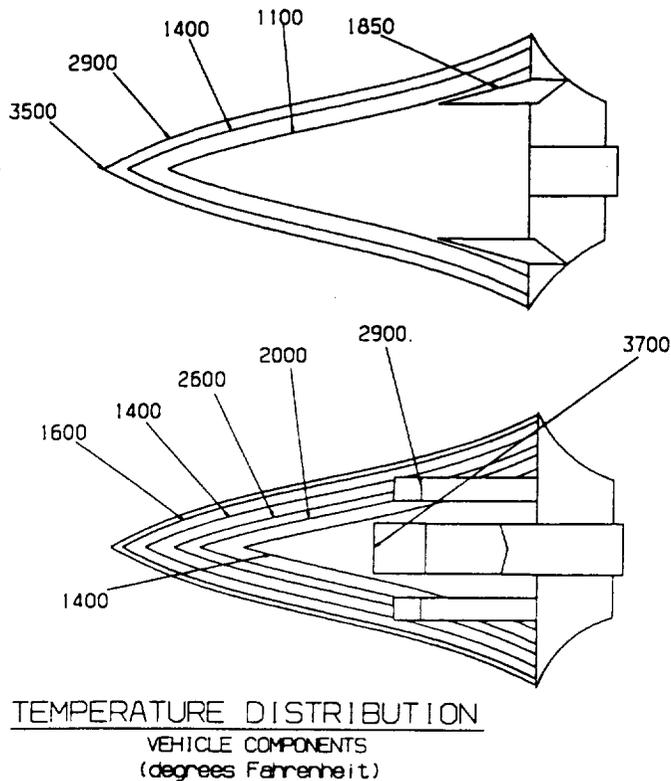
It must also be mentioned that the skin temperatures were
calculated assuming that the materials have reached steady state.

Matt Mellis, a heat transfer scientist at NASA Lewis Research Center in Cleveland, Ohio, also suggested that in some cases the materials would reach steady state in about 0.7 seconds.

Based on the melting temperatures of most alpha-beta type Titanium alloys, it was determined that the viable working temperature for the materials was around 1200 degrees Fahrenheit. Since this is an experimental aircraft it was deemed allowable to work at the very limits of the material. Therefore, it is necessary to actively cool the surfaces at temperatures above 1200 degrees Fahrenheit. The decision was made to use some type of Nickel based superalloy bonded with the Titanium in order to exploit the high emissivity of these alloys, which is on the order of 0.89. This emissivity was used when developing the temperature distribution program so that the aircraft could radiate heat at a rapid rate.

The output of the program and the skin distribution diagrams (see Figures 7.1 through 7.3), shows that the aircraft will have to be actively cooled 34 feet back from the leading edge on the bottom surface, 10 feet from the leading edge on the top surface, at the inlets, and over all of the vertical control surfaces.

7.2 Materials:

Studying the output from the CDHEAT program (see Appendix C), it is obvious that few materials can withstand the high temperatures experienced by the aircraft. The materials at the nose and leading edge must exhibit good thermal loading, high

creep resistance, and, if possible, reusability. Most carbon-carbon composites can meet the thermal requirements, but the carbon-carbon composites evaluated for the nose cap exhibited oxidation erosion at the temperatures experienced requiring the nose cap to be replaced after each flight. A JTA composite (a composite that contains traces of zirconium, silicon, and boron in addition to carbon) forms a protective coating on the outer surface as it oxidizes, greatly reducing the oxidation erosion, and thus increasing the thermal loading life of the composite. (Reference 21) The maximum working temperature of JTA is approximately 4000 degrees Fahrenheit. Upon further investigation, it was estimated that the JTA composite could last up to 25 flights before it would need replacing. Compared with the carbon-carbon composites requiring replacement after each flight, the JTA composite proved superior and was therefore chosen as the material for the nose cone.

A durable and reusable high temperature carbon-carbon heat pipe structure was used as the material for the leading edge. This design uses refractory metal heat pipes embedded within a carbon-carbon structure, with the carbon-carbon acting as the primary load carrying part of the structure. This system is discussed in detail in Section 7.3. Due to the extremely high temperatures experienced by the vertical stabilizers, all control surfaces will be made out of the carbon-carbon heat pipe structure.

In order to exploit the advantages of radiative cooling, a

material with a high emissivity had to be chosen for the outer skin. Upon investigation, Hastelloy-X (22Cr-18Fe-9Mo-1.5Co-.5W Nickel Alloy) was chosen as the most promising material having an emissivity of approximately .89 at the temperatures the aircraft experiences. Hastelloy-X also displayed excellent oxidation and useful creep resistant properties. Hastelloy-X actually forms a tightly adherent oxide scale which does not spall off and retains its strength at heightened temperatures.

Although Hastelloy-X displayed excellent thermal properties, it was lacking as a structural material with a considerably lower yield strength and strength to weight ratio than a titanium alloy (at elevated temperatures, the yield strength for the Nickel alloy was approximately 8,000 psi compared to a yield strength of 75,000 to 90,000 psi for alpha-beta titanium alloys at similar temperatures). For this reason, it was decided to bond the two materials together, in order to combine the thermal superiority of Hastelloy-X with the high strength to weight ratio of a titanium alloy. The titanium alloy of choice is Ti-6Al-4VELI which displays the required characteristics, and because it is the most commercially available titanium alloy. This particular titanium alloy is similar to standard Ti-6Al-4V except it is superior in fracture toughness and weldability. Due to the high emissivity of the nickel alloy, the active cooling system needed to cover a 60% smaller area than if only a titanium alloy were used on the outer skin. For this reason, a metal composite skin was used for this aircraft.

The method of bonding the two alloys together is known as explosive welding (see Figures 7.4 and 7.5). In explosive welding there is a high velocity oblique impact between the components being welded which causes the metals to behave like fluids. As a result a high velocity jet is formed from the surfaces of the components, which leaves two virgin clean surfaces which are pressed together to form a weld. This weld actually acts as a bond on the molecular level, producing a bond even stronger than the original materials. Explosive welding joins two (or more) metals achieving virgin surfaces without oxides or other contaminant surface films, preserving the material properties. (Reference 22).

Figure 7.4: Explosive Welding of Composite Skin

Figure 7.5: Plates Joined in Explosive Welding
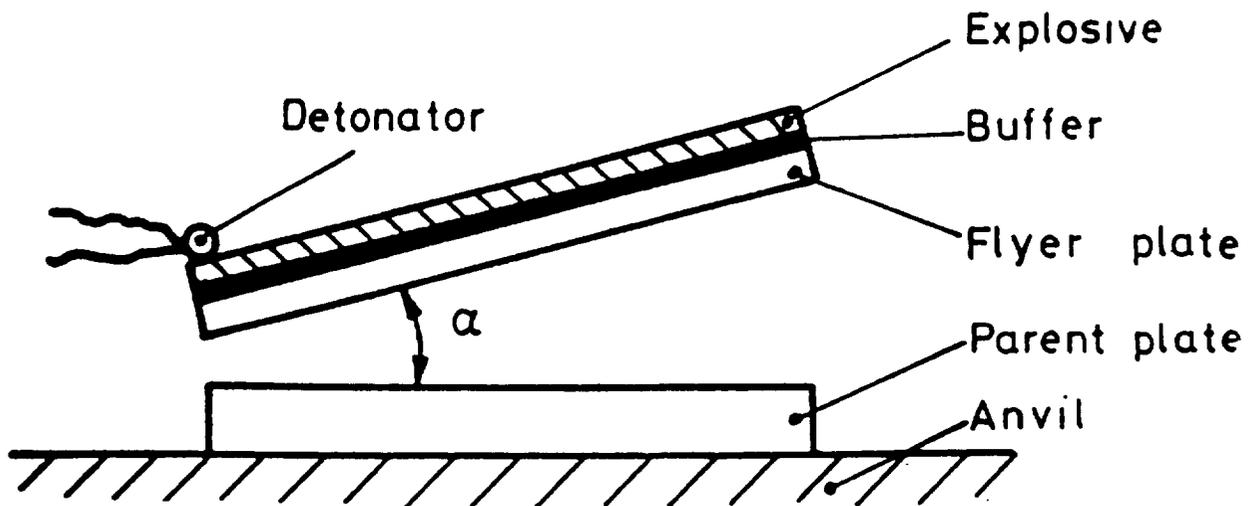
Figure 7.5: Plates Joined in Explosive Welding
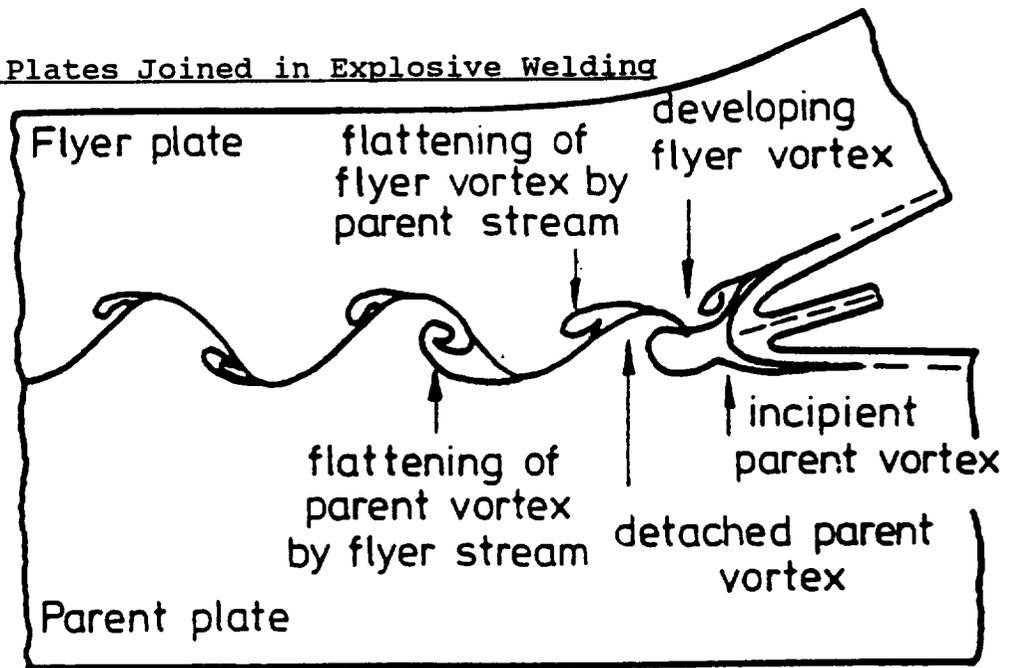
An initial stress analysis using Hooke's Law was completed to determine the thermal stresses due to thermal expansion. The results show a small margin of safety based on the yield strength of the titanium alloy and were therefore deemed acceptable. In order to increase the durability and life of the bonded alloys, a thin layer of niobium or columbian must be placed between the nickel and titanium to act as a buffer between bonds at the molecular level. The outer skin was therefore modelled as a microstructural isotropic layer of three thin metal foils. (Reference 9).

Due to the extremely high temperatures and the mechanical nature of the inlets, the decision was made to fabricate the inlets out of the Hastelloy-X / Ti-6Al-4V composite skin. The mechanical integrity of the material depends on the cooling system of choice. The proposed material for the inlets are fabricated honeycomb panels (see Figure 7.6). Honeycombs can

also be produced by explosive welding. As described in Reference 22, the fabrication of honeycomb by explosive welding is attractive, and have been produced in a wide range of materials, including titanium and hastelloy. The 'hot spot' or stagnation point, of the inlet experiences temperatures of approximately 3700 degrees Fahrenheit. In order to control the reflection of the shock as it impinges at this point, it was necessary to make the radius of curvature as small as possible resulting in high wall temperatures. Therefore, to meet the thermal requirements, the material at the leading edge of the inlets will be the JTA graphite composite which can operate at temperatures up to 4000 degrees Fahrenheit. It was estimated that the leading edge of the inlets would have to be replaced every 20 flights. By choosing JTA, the cooling requirements were reduced considerably and the integrity of the design was ensured.

Figure 7.6: Explosive Welding of Honeycomb Structure

printed strips to prevent welding
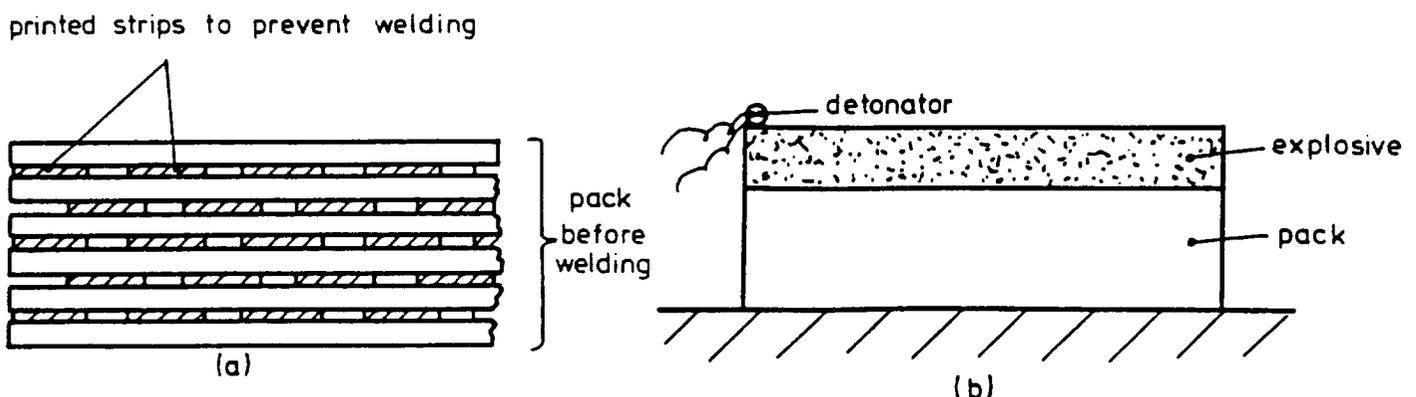
7.3 Cooling System:

The only cooling systems considered were those systems that could maintain skin temperature levels at or near the viable working temperatures of the materials used.

Three types of cooling systems were examined. The first was transpiration cooling. Transpiration cooling is very desirable since it actually introduces a coolant into the boundary layer increasing the aerodynamic performance of the aircraft. This coolant acts as a layer of insulation between the hot boundary layer and the skin of the aircraft. It was initially decided that transpiration cooling would be used since enough coolant for a short flight of approximately 10 to 15 minutes would be required. Since then, however, the mission profile has dictated a longer flight time. It is now necessary to cool for about 40 minutes (cooling will have to start after Mach 4 and continue until landing). With this in mind, it was determined that the required coolant would become too cumbersome and would have to be replaced after every flight. This increase in weight and cost eliminated transpiration cooling as a feasible system.

Next, convective cooling using the hydrogen as a coolant was studied. The argument in favor of hydrogen is as follows: since hydrogen is already on board, why not use it as a coolant? This is a valid argument since hydrogen provides a fine heat sink. However, being a manned vehicle, the complicated pumping systems involved to keep the hydrogen cooled and circulating around the entire aircraft would become too heavy and extremely dangerous

for the pilot. It has been decided, however, to regeneratively
cool the inlets and engines using the hydrogen fuel. Referring
to Figure 7.7, this would involve pumping the hydrogen through a
heating jacket in the engine inlets and nozzle regions. The
hydrogen then flows toward the throat of the engines, where it is
collected in manifolds and directed toward the fuel plenum. From
there, the hydrogen is routed to manifolds in each strut and
injected into the airstream. (Reference 11)

Figure 7.7: Regeneratively Cooled Inlets
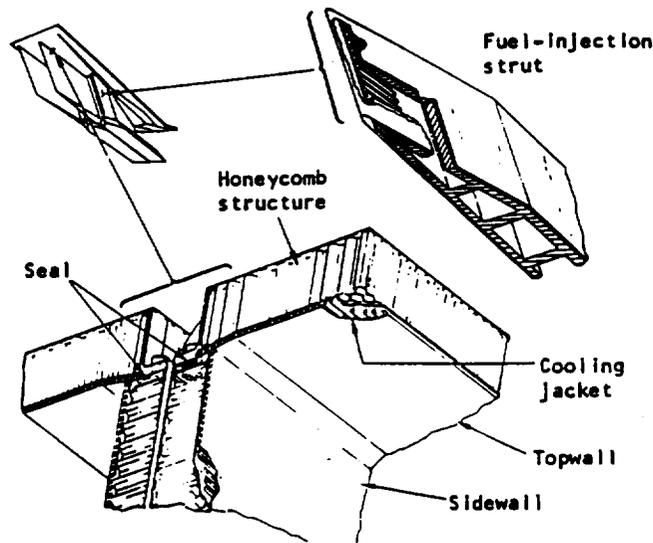
The last type of cooling method considered was a convective
cooling system using a separate coolant. For longer flights this
would seem the best alternative to using hydrogen. Since the
coolant would be denser than the fuel, it would require a much
lower flow rate. Two types of convective cooling systems were
considered. The first was spray cooling, where the coolant is
actually injected against the inside wall of the aircraft, and is
pumped back through separate ducts. The second involves a

66

coolant flowing through pipes placed as close as possible to the leading edge of the aircraft. There it acts as a heat sink for the skin of the aircraft, where the energy of the skin is transferred in the form of heat into the coolant. In both of these cases, the coolant is then pumped back to a heat exchanger where hydrogen fuel, prior to being injected into the airstream, acts as a heat sink for the coolant and is therefore preheated before injection. Spray cooling was not chosen since little literature is available on obtaining quantitative values for this system (most of the details are unavailable to the general public).

As stated in Section 7.2, a durable and reusable high temperature carbon-carbon heat pipe structure was used at the leading edges to actively cool the leading edges. The pipes are routed through the body of the plane and are eventually integrated into the leading edge structure. This system operates at temperatures up to 2800 degrees Fahrenheit in an oxidizing environment, and coatings currently under development will extend the maximum temperatures to above 3000 degrees Fahrenheit. The embedded heat pipes remove high local heat from the leading edge where it is in turn removed by the heat exchanger. The heat pipes help to eliminate local hot spots and associated thermal gradients, to reduce stresses and to reduce peak surface temperatures of the carbon-carbon to levels within the capability of the oxidation resisting system.

Since the maximum structural reuse temperature of carbon-

carbon is much higher than that of refractory metals or superalloys, this concept requires less area for radiation and consequently weighs much less.

The most attractive refractory metal for fabrication of heat pipes is tungsten because of its compatibility with liquid metal working fluids, its low rate of reaction with carbon, and its good mechanical and thermophysical properties at high temperatures, and its low coefficient of thermal expansion. The coefficient of expansion is close to that of carbon-carbon, thereby minimizing thermal stresses. Figure 7.8 shows the diagram of the leading edge cooled by the metal heat pipes integrated into the carbon-carbon structure of the leading edge.

<u>Figure 7.8: Leading Edge Heat Pipe Structure</u>
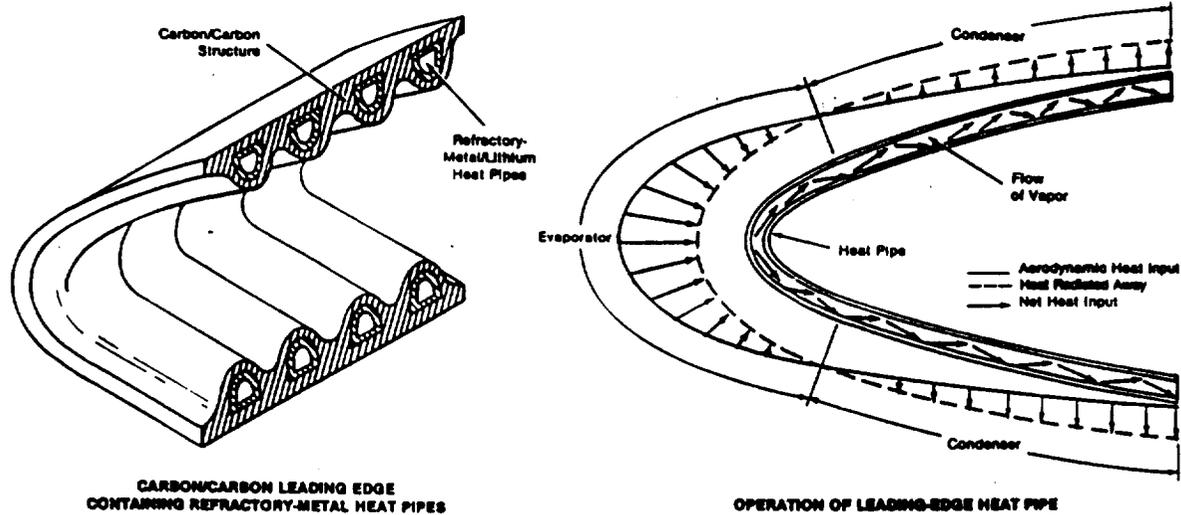
Having determined the type of cooling system, the next step was to find a coolant that would minimize both the coolant flow rates and the heat exchanger and pump weights. By using the temperature distribution, dividing the aircraft into 250 separate

areas, and determining the average temperature for each area, the method described in Appendix C was used to determine the weights and fuel flow rates for the convective cooling system. Assuming that no cooling was required for temperatures over 1200 degrees Fahrenheit, lithium, with its high specific heat of .996 BTU/lb-°F and stability up to coolant temperatures of 1350 degrees Fahrenheit, was chosen as a coolant. Liquid silicon and water glycol were eliminated as possible coolants since they are unstable at coolant temperatures above 400 and 200 degrees respectively. Sodium was also considered, but its low specific heat of .302 BTU/lb-°F tripled the coolant flow rate and doubled the heat exchanger and pump weights when compared with lithium. Table 7.1 outlines the final values for coolant flow rates, fuel flow rates required for cooling, and system weight. The values in this table reflect both the results for regenerative and convective cooling. It is important to note that the fuel flow rate required for cooling does not exceed the fuel flow rate required for the engines. However, the cooling requirements during the unpowered deceleration from Mach 10 to landing require that extra fuel be carried just for cooling during this phase. A schematic of the cooling system routing is shown in Figure 7.9.

Table 7.1: Liquid Convective Cooling System Specifications

Systems (skin)   Convective Cooling with Lithium
          (inlets)   Regenerative Cooling with Hydrogen

__Weights__
Heat Exchanger   860 lbs
Distribution System   1320 lbs
Lithium   500 lbs
Pumps   __1000 lbs__
                              TOTAL   3680 lbs

Max. Coolant Flow Rate   4300 lb/hr
Max Fuel Flow Rate   3600 lb/hr

Figure 7.9: Cooling System Schematic
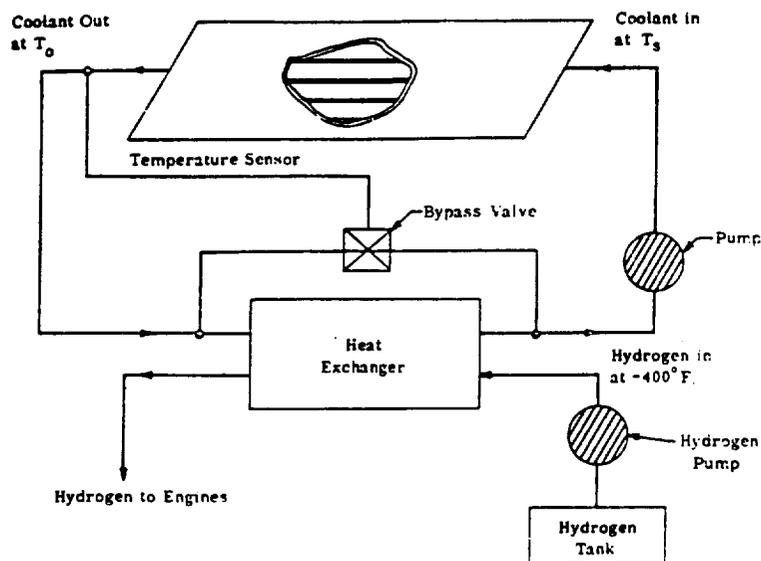
7.4 Hydrogen Fuel Tanks and Insulation System:

The primary purposes of the hydrogen tank insulation system
is the minimization of hydrogen boil off, the minimization of the
thickness and weight of the insulation system, the prevention of
liquification of surrounding gas on the tank surface
(cryopumping)[1], and prevention of moisture condensation or

---

[1]   Experiments have shown that the resulting cryopumping
action can release heat at a rate as high as 3600 Btu/hr-ft^2, which
represents a fuel boil-off rate of 18 lb/hr-ft^2 -- a totally

freezing. It is possible to completely insulate the system to prevent all boil off, but the thickness and weight involved would be impractical for aerospace applications.

An inert purge system was used in that portion of the aircraft which contained the tankage. Purging will prevent the accumulation of hydrogen which may leak through the tank walls or system lines and condensation of air and moisture which might otherwise come in contact with the cryogenic tank. The purge gas also fills the area with a low thermal conductivity gas which helps in the insulation process.

Since the aircraft is to be actively cooled, the tanks have to be insulated from average wall temperatures above 1000 degrees Fahrenheit. Active cooling, however, allows for thinner insulation to be used reserving the space for other uses.

Two sealed systems were considered: one was a cryoevacuated plastic foam that is sealed with a Mylar film, and the other is an evacuated foil insulation that is sealed with a welded foil cover skin. The sealed systems offer a potential for less weight than the purge systems, but reliability is a problem. As indicated by Heathman and Kelley (Reference 18), the plastic foam system has been dropped from further study because of difficulties in maintaining a seal. Attempts at fabrication of the foil system have met with similar results, and it appears that welded evacuated leak free construction of foils is beyond state of the art. (Reference 16)

---

unacceptable rate for a flight vehicle (Reference 19).

Three types of purge systems were also considered: a nitrogen purge sealed insulation system, a helium purge non-sealed fibrous insulation, and a carbon dioxide purge system with a non-sealed fibrous insulation. A typical quartz fiber material, Microquartz, with a density of 3 lb/ft^2 was selected.

The nitrogen gas would have to be used externally to the sealed foam insulation because the gas would condense at liquid hydrogen temperatures. To prevent the liquification of the nitrogen gas, a sealed system would have to be designed so that all surfaces in contact with the nitrogen were above 160 R.

Although the nitrogen offers the lightest possible foam insulation system, the system would require that an additional tank of nitrogen be carried along to supply the insulation system with nitrogen. The additional weight of the tankage and distribution system, along with the fact that the sealed foam insulation has not proven to be effective over many fillings of the cryogenic tanks, eliminated nitrogen purge as a possible insulation system.

The helium purge system uses noncondensable helium purging, but helium has a high thermal conductivity at the purge gas pressure required during flight and would require an extra tank to replace the helium boil off. The additional weight for the purge system (helium and its containers) leads to a higher system weight than either nitrogen or carbon dioxide purge systems.

The carbon dioxide system was selected because of its many distinct advantages. Carbon dioxide gas was selected because of

its low thermal conductivity, preventing purge gas boil off, and its lack of a liquid phase at the pressures and temperatures encountered. Figure 7.10 illustrates a carbon dioxide system on a hydrogen fueled hypersonic aircraft. Figure 7.11 shows a schematic of the carbon dioxide thermal protection system for the lower tank surface. The frost is cryodeposited within the inner thickness of a fibrous insulation on the tank walls during ground hold before each flight. Initially, as a result of reduced pressure with increased altitude, and by aerodynamic heating, the frost sublimes providing a continuous supply of purge gas which flows outward through the insulation and prevents inflow air through the structure. The low thermal conductivity of the gas and of the frost, plus the heat absorption capability of the subliming frost and of the transpiring carbon dioxide gas through the insulation result in a low fuel heat load during flight. Thus, the carbon dioxide purge system not only prevents cryopumping of air to the cold tank walls, but also results in a low fuel boil off.

Figure 7.10: Carbon Dioxide Purge Insulation System

STRUCTURE-UNSEALED

CO_2 PURGE GAS

FIBROUS INSULATION

TANK WALL

CO_2 FROST
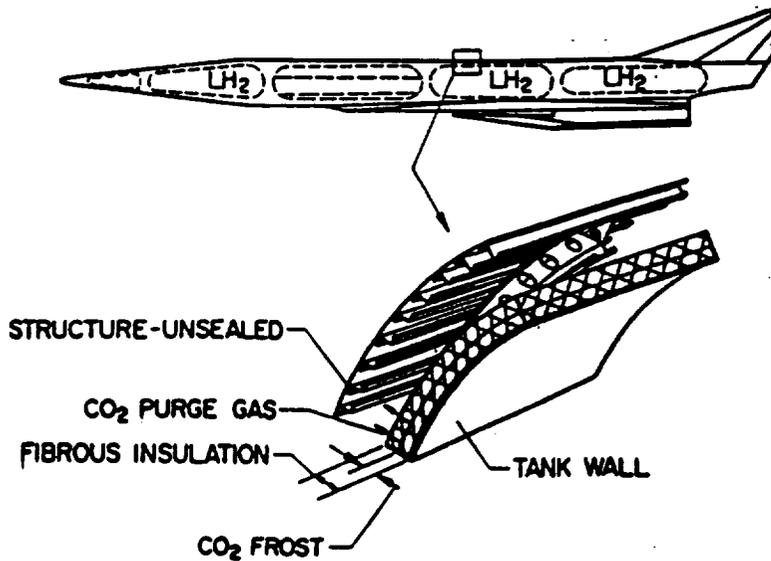
Figure 7.11: Carbon Dioxide Lower Surface Insulation

LOWER TANK SURFACE

LIQUID HYDROGEN

X_I

X_O

X

T_I

T_s

T_o

CO_2 FROST

FIBROUS INSULATION
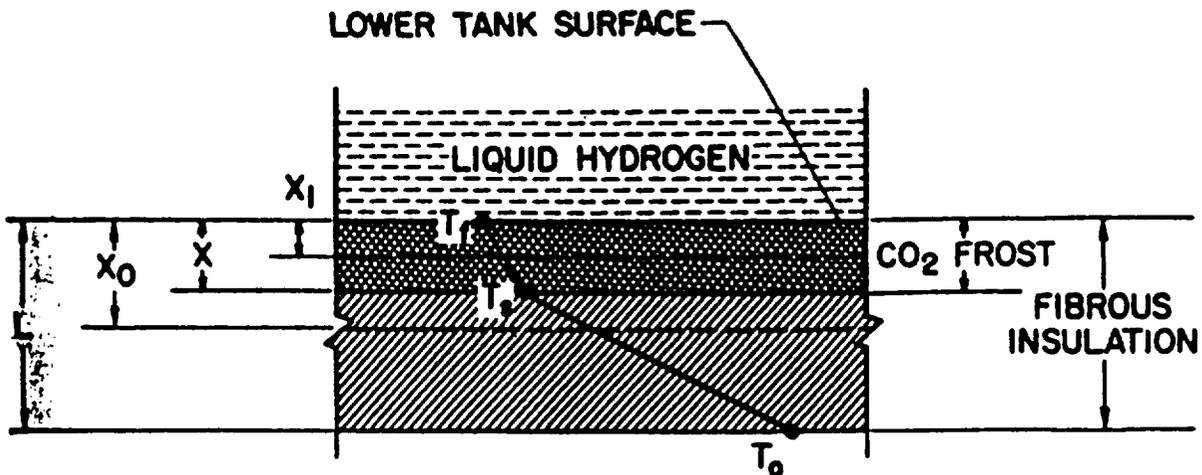
Low density carbon dioxide provides resistance to cryopumping flow, permitting sufficient time for the carbon dioxide to freeze before particles make contact with the frost deposit. Moreover, as the carbon dioxide solidifies, each particle is surrounded with a film of the noncondensable gas that remains around the particle to result in a deposit of frost.

The fuel tanks are made out of .06 gage 5Al-2.5Sn Titanium Alloy to prevent the hydrogen embrittlement. This particular titanium alloy has an extra low interstitial grade and has an excellent combination of toughness and strength at cryogenic temperatures (-437 F). The tanks are filled to an initial pressure and temperature of 17 psia (1.15 atm) and 37 degrees Rankine (-437 F) respectively along with a venting pressure of 25 psia (1.7 atm). These pressures are developed from the hydrogen within the tanks, therefore no external pressure device is needed. It must be noted that the weight estimate is based solely on the outside skin only and does not include fuel lines, hydrogen pumps, or inside baffle weights.

A breakdown of the insulation and tank weights is shown in Table 7.2. Appendix C describes the methodology in estimating the thicknesses and weights of the carbon dioxide purge system. Since the tanks are to be topped off with hydrogen in flight, there are no results for hydrogen boil off during ground hold.

Table 7.2: Insulation and Tank System Specifications

Tank Material	.06 gage 5Al-2.5Sn Titanium Alloy
Tank Pressure (initial)	17 psia (1.15 atm)
(venting pressure)	25 psia (1.70 atm)
Internal Temperature	37 R (-437 F)
Exposure Time	50 minutes
Exposed Area	550 ft^2
Insulation System	Carbon Dioxide Frost
Insulation Thickness (Forward)	2 in
(Aft)	1 in

Weights
Boil off	900 lbs
Insulation System	1300 lbs
Tanks	825 lbs
TOTAL	3025 lbs

Section 8:   Cost Analysis

A general cost analysis was performed for the SCET aircraft
program using empirical formulas derived from the cost of past
aircraft (Reference 6). Since this is an experimental test
aircraft, the analysis includes only the cost of development and
two test aircraft. The number of aircraft was set at two to
provide one aircraft for flight verification and a second for
extensive SCRAMjet testing. Additionally, aircraft not being
tested at any given time can be modified to allow changes to the
SCRAMjet and instrumentation. This will allow greater
variability for the test without causing large delays in testing.
A cost breakdown is provided in Table 8.1.

Table 8.1:   Cost Analysis Breakdown (2 Aircraft)

	Cost (Billions)	
Airframe Engineering	2.02	
Development Support	1.62	
Flight Test A/C	0.63	
Flight Test Operations	0.08	
Subtotal	4.35	
10% Profit	0.44	
Total	4.79	(1990 Dollars)

It is obvious, and not surprising, that the majority of the
cost involved is for engineering and development. Since the data
was derived primarily from aircraft to be used in production,
these cost estimates may be low. More money may be required for
basic research to bring some of the necessary technologies up to
the point where they can be applied to an aircraft system. It is
difficult, though, to separate which development costs are for

basic research and which should be billed to a specific program. In this light, the cost given should be realistic given that research money is available from other sources as well.

Section 9: Conclusions

The design goals of the Supersonic Combustion Engine Testbed (SCET) have been met. This simple sentence conveys much more than just that the initial design criteria have been fulfilled. It shows that the basic goal of the mission is possible; hypersonic flight using SCRAMjet propulsion is feasible. Along the way many difficult obstacles were overcome. An efficient aerodynamic shape was found. Multiple propulsion systems and a large fuel volume were successfully integrated into the aircraft. And, the difficult problem of aerodynamic heating was solved. In addition, the technologies used will available when SCRAMjets are ready for flight testing.

Production of the SCET will not be cheap or easy. Many technologies must make the crucial step from the laboratory to the field for the program to be a success. But, the principle of the SCET program is not just to see if these steps can be made. A commitment to these technologies has already been made by such programs as the National Aerospace Plane (NASP). More fundamental is the need to encourage these steps as soon as possible to stimulate the interest, excitement, and foundation necessary to complete such ambitious projects as the NASP.

References

1. NASA TN D-6692; Mark D. Aroema; March 1972

2. K. G. Bowcutt, J. D. Anderson, D. Capriotti, "Viscous Optimized Hypersonic Waveriders", AIAA-87-0272

3. Louis D. Williams, "Estimated Aerodynamics of All-Body Hypersonic Aircraft Configurations" NASA TM-2091

4. Stephen Corda, "Viscous Optimized Hypersonic Waveriders Designed from Flows over Cones and Minimum Drag Bodies", January 1988

5. Stephen Corda, "User Information for Maryland Axisymmetric Waverider Program", June 1987

6. Leland M. Nicolai, Fundamentals of Aircraft Design, 1975

7. J. D. Anderson, Modern Compressible Flow, 1982

8. J. D. Anderson, Introduction to Flight, 1985

9. HyBuJet

10. "Conceptual Design Aerodynamic Heating Analysis" (CDHEAT)

11. Buchmann, O. A., "Thermal-Structural Design Study of an Airframe-Integrated SCRAMjet," NASA CR-3141, October, 1979.

12. McConarty, W. A. and Anthony, F. M., "Design and Evaluation of Active Cooling Systems for Mach 6 Cruise Vehicle Wings," NASA CR-1916, December, 1971.

13. Helenbrook, R. G., McConarty, W. A. and Anthony, F. M., "Evaluation of Active Cooling Systems for a Mach 6 Hypersonic Transport Airframe," NASA CR-1917, December, 1971.

14. Kreith, Frank and Bohn, Mark S., Principles of Heat Transfer, 4th Edition, Harper & Row, Publishers, Inc., New York, New York, 1986.

15. Khol, Ronald, editor, 1987 Materials Reference Issue, Machine Design, April 16, 1987.

16. Jackson, L. R. and Anderson, M. S., "A Carbon Dioxide Purge and Thermal Protection System for Liquid Hydrogen Tanks of Hypersonic Airplanes," Advances in Cryogenic Engineering, Vol.12, Timmerhaus, K. D., ed., Plenum Press, New York, New York, 1967.

17. Camarda, Charles J. and Ransone, Philip O., "Carbon/Carbon Panels Cooled by Heat Pipes," NASA Tech Briefs, July, 1989.

18. Heathman, J. H. and Kelley, L. G., "Hydrogen Tankage for Hypersonic Cruise Vehicles," Volume of Technical Papers presented at AIAA/ASME Seventh Structures and Materials Conference, Cocoa Beach, Fla., April, 1966.

19. McGrew, J. L., in: Advances in Cryogenic Engineering, Vol.8, Plenum Press, New York, New York, 1963, p.387.

20. Aerospace Structural Metals Handbook, Vol. 3 & 4, Department of Defense, Mechanics Research Center, Watertown, Mass., 1975.

21. Stein, Bland A., Illg, Walter, and Buckley, John D., "Structural Materials for Hypersonic Aircraft," Chapter 28 of NASA SP-148, Compilation of papers presented at a Conference on Hypersonic Aircraft Technology, May, 1967.

22. Crossland, Bernard, Explosive Welding of Metals and Its Application, Clarenden Press, Oxford, 1982.

23. Air Force Systems Command, Crew Stations and Passenger Accommodations

Appendix A

Appendix A: Subsonic Wind Tunnel Test

In order to verify the subsonic characteristics of this aircraft, a subsonic wind tunnel model was built for testing in the Ohio State 3 foot by 5 foot subsonic wind tunnel. The model was built to 1/72 scale, which is approximately two orders of magnitude smaller in Reynold's number.

The model was constructed of several types of wood and epoxy. The main body was constructed out of a solid block of willow, and the vertical stabilizers and turbofan-ramjets were made of balsa wood. All of the leading edges and the TFRs were coated with epoxy and then sanded to shape. This allows greater strength, greater durability, and a better finish than could be obtained by just using wood. The mount for the sting was made of aluminum and recessed in the model such that it could be completely covered by the mock SCRAMjet modules. A single set screw holds the model to the sting when it is mounted in the tunnel. The model was painted with approximately ten coats of flat black enamel, and then was coated with six coats of polyurethane for a durable, smooth finish.

The total time involved in making this model was approximately forty hours. The total cost of materials was approximately twenty-five dollars. The equipment used consisted of a bandsaw, an electric drill, a belt sander, a dremel, chisels, files, and sandpaper.

As was stated above, the testing was done in OSU's 3'x5'

subsonic tunnel. A strain gage balance was used which allowed measurements for axial force, normal force, and pitching moment. The maximum measurable values were 20 lbs., 6 lbs., and 32 in.-lbs., respectively.

The testing procedure went as follows. The balance was set up in the tunnel and connected to the switch and balance box and digital voltmeter as shown in Figure A.1. The power to the switch box was then turned on so that the resistors would be warm when the testing was done. A Pitot probe was connected to a water manometer for the purpose of determining the tunnel velocity. Next, the model was mounted on the sting such that the wings would be perpendicular to the bottom of the tunnel. A level was used to make sure the model was not mounted with any degree of roll. Then, with the top surface of the model chosen as the longitudinal reference line (the top surface is straight), measurements were taken from the tunnel edge in an attempt to get the model set parallel to the tunnel. The pointer was fixed to the balance shaft pointed at zero degrees angle of attack. The tunnel was then closed up in preparation to run. The balance was zeroed for all three properties being measured. The ambient pressure and temperature were recorded for later use, and the tunnel was started and allowed to reach steady state. The Pitot pressures were recorded from the manometer, and the voltages for the three properties were recorded for zero degrees angle of attack. The model was then rotated to two degrees and the data was recorded. This procedure was repeated every two degrees

until the balance limits were reached or the model stalled.

Figure A.1:   Wind Tunnel Test Setup
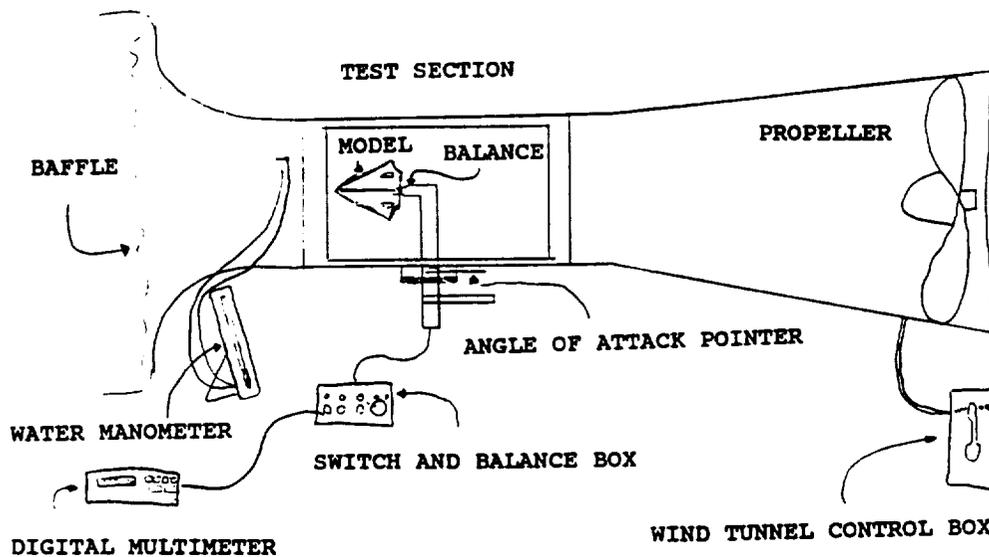
The model was tested at two velocities in the tunnel; one at 144 ft/sec, and one at 119 ft/sec. These velocities correspond to 100% and 80% power, respectively, for the wind tunnel propeller at a blade pitch setting of 12 degrees. The resulting data is shown in Tables A.1, A.2, and A.3. Due to the delta shape of this aircraft, it was assumed that the model would stall at a very high angle of attack. Unfortunately, due to the limits on the balance, it was not possible to find the stall point at the two velocities shown.

84

Table A.1: Wind Tunnel Data Run #1

Velocity = 144 ft/sec   Q = 23.85 psf   Re = 1,108,000

Alpha	C_l	C_d	C_m
0	0.1247	0.0444	0.2012
2	0.1994	0.0491	0.3278
4	0.2892	0.0737	0.4799
6	0.3648	0.0992	0.5961
8	0.4489	0.1351	0.8021
10	0.4687	0.1616	1.0969
12	0.5415	0.2164	1.3529
14	0.5774	0.2741	1.5598
16	0.6785	0.3478	1.7790

Table A.2: Wind Tunnel Data Run #2

Velocity = 119 ft/sec   Q = 16.29 psf   Re = 915,000

Alpha	C_l	C_d	C_m
0	0.1384	0.0443	0.2159
2	0.2048	0.0512	0.3596
4	0.2864	0.0719	0.4855
6	0.3625	0.0982	0.5920
8	0.4386	0.1314	0.7608
10	0.5092	0.1701	0.9503
12	0.5244	0.2006	1.2601
13	0.5562	0.2269	1.3652
15	0.5936	0.2836	1.5907
16	0.6392	0.3182	1.6474
18	0.7389	0.3943	1.8521
20	0.8150	0.4690	2.0361
22	0.8910	0.5534	2.2284
24	0.9838	0.6534	2.4013

Table A.3: Wind Tunnel Data Run #3

Velocity = 123 ft/sec   Q = 17.18 psf   Re = 934,000

| Alpha	C_l	C_d	C_m
-8	-0.1244	0.0291	0.0170
-6	-0.0519	0.0244	0.0410
-4	0.0122	0.0221	0.0388
-2	0.0645	0.0274	0.0901
0	0.1295	0.0355	0.1706
4	0.2724	0.0733	0.4064
8	0.4524	0.1366	0.6694
12	0.5374	0.2103	1.1403
16	0.6299	0.3212	1.4678
20	0.8296	0.4788	1.8144
24	0.9679	0.6516	2.1268

Appendix B

Appendix B: Shock Expansion Calculations

The following discussion presents the program which was
written to determine the supersonic lift and drag on the
waverider aircraft. The program was written using shock-expansion
theory. The reason for choosing this method was the fact that a
waverider has a unique geometry which lends itself well to this
kind of approximation.

A basic waverider body is unique in that the geometry of
every longitudinal cross section is the same. This means that
the angle at the leading edge, here called phi, is constant for
the entire aircraft.

For easier calculation, the aircraft was broken up into
three constant geometry cross sections. The aircraft was split
in half, and each half had three different constant airfoil
sections (see Figure B.1). One section was the area of the wing
outboard of the turbofan-ramjets (TFRs). Another section was the
area of the wing between the TFR and the SCRAMjets. The final
section was that containing the SCRAMjets. The process for
finding the lift and drag was the same for each of the cross
sections so this discussion will mainly cover a single section.
A section has four faces, each face having a specific surface
area. The purpose of the program was to determine the pressure
on each of the faces and resolve these pressures into forces.
All equations used were obtained from compressible flow text
written by Dr. John D. Anderson.

Figure B.1: Airfoil Cross Sections

airfoil section 1

airfoil section 2
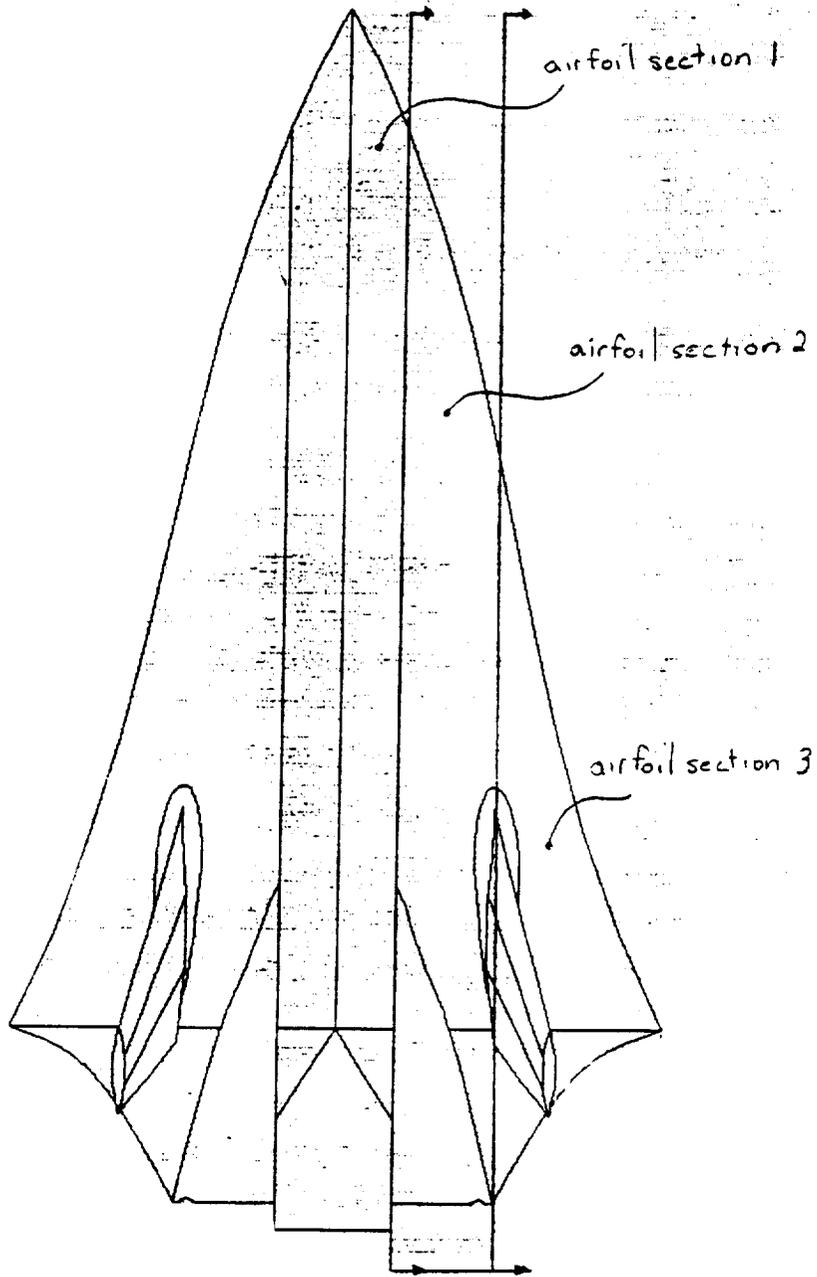
airfoil section 3

The top-front surface of the airfoil section was chosen as the zero reference line to simplify calculations. A restraint in the program limited the minimum angle to the value negative phi. The free stream conditions were designated as region 1. Three situations were found to occur depending on the angle of attack being used. The first situation was that where the angle of attack was less than zero (Figure B.2a). This situation would cause oblique shocks to occur in front of both regions two and three. Isentropic expansions would then occur in front of regions four and five. The second situation occurs when the angle of attack equals zero (Figure B.2b). The oblique shock remains in front of region three, but the one in front of region two disappears. The conditions in region two are now equivalent to those in region 1. The expansions remain in regions four and five. The third situation occurs when the angle of attack is greater than zero (Figure B.2c). Region three retains its oblique shock, but now region two has an expansion preceding it. Regions four and five remain as before.

Figure B.2:   Shock Expansion Reference Angles

- Case 1, x < 0

Region 1

oblique
shocks

x < 0

Region 2

$\theta_2 = \alpha$ $P_2, A_2, M_2, \nu(M_2)$

$\theta_3 = \phi - \alpha$

$P_3, A_3, M_3, \nu(M_3)$

Region 3

expansion

Region 4

$P_4, A_4, M_4, \nu(M_4)$

ψ

expansion

Region 5

$P_5, A_5, M_5, \nu(M)$

- Case 2, x = 0

Region 1

$\alpha = 0$

Region 2

$\theta_3 = \phi$

Region 3

Region 4

Region 5

- Case 3, x > 0

Region 1

x > 0

Region 2

$\theta_3 = x + \phi$

Region 3

Region 4

Region 5

89
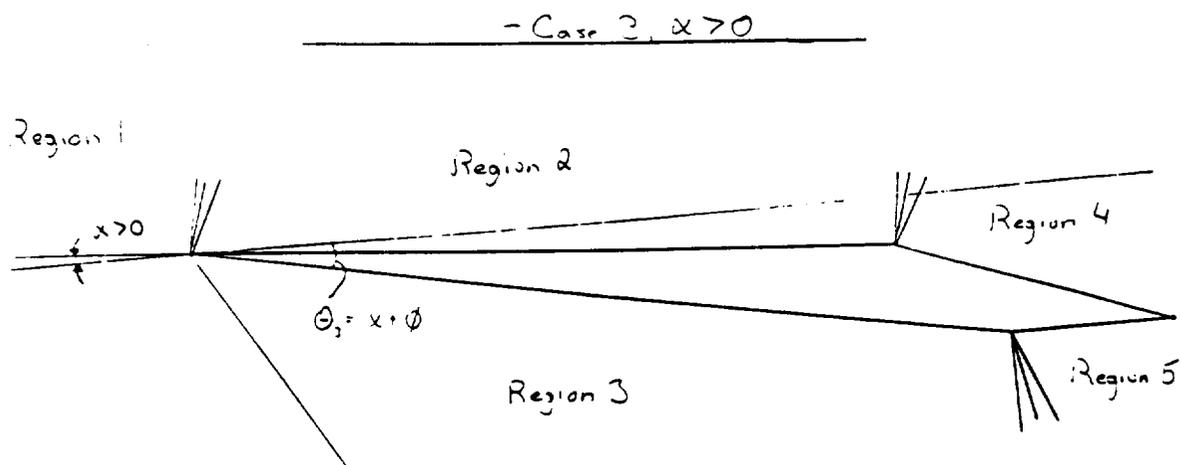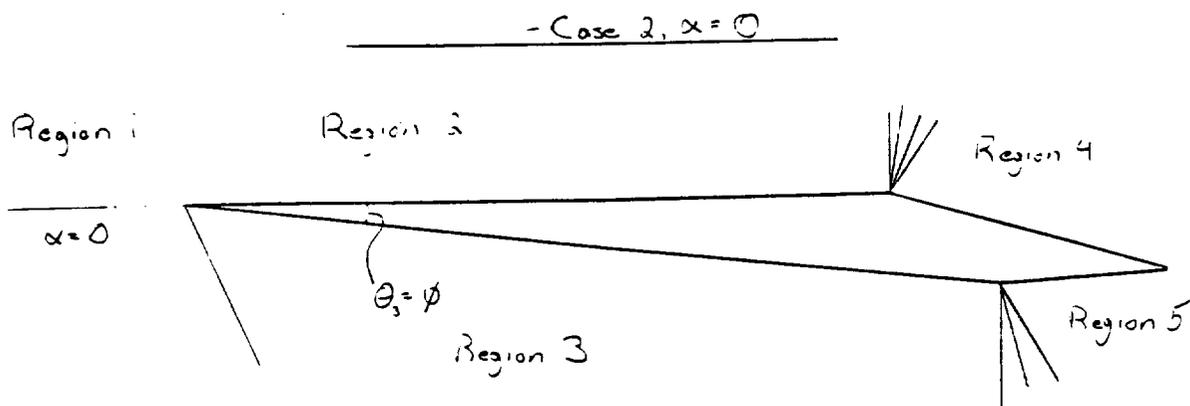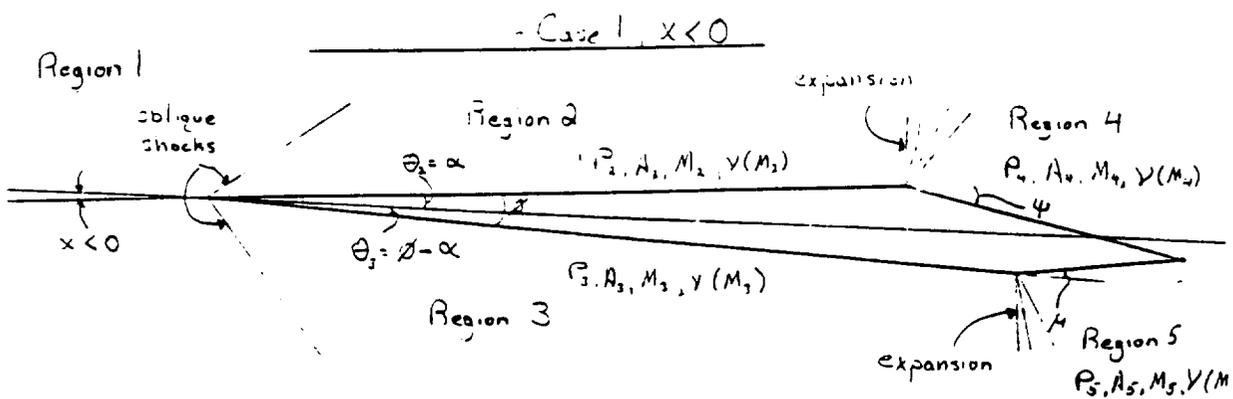
For the regions where an oblique shock occurred, subroutines were written to calculate the shock angle and flow properties downstream of the shock. The first subroutine was that which calculated the shock angle. This was done using the following formula:

$$\theta = \arctan\left[\frac{2}{\tan\beta}\left(\frac{M_1^2 \sin^2\beta - 1}{M_1^2(\gamma + \cos 2\beta) + 2}\right)\right]$$

Theta and the Mach number are both known, but Beta must be calculated. Since this equation cannot be solved explicitly for Beta, an iteration routine was set up.

Another subroutine was set up to calculate the flow properties downstream of the shock. The following equations were used:

$$P_2 = P_1\left(1 + \frac{2\gamma}{\gamma+1}\left(M_{n_1}^2 - 1\right)\right) \qquad P_{0_2} = P_2\left(1 + \frac{\gamma-1}{2}M_2^2\right)^{\frac{\gamma}{\gamma-1}}$$

$$M_{n_2} = \sqrt{\frac{M_{n_1}^2 + \left(\frac{2}{\gamma-1}\right)}{\frac{2\gamma}{\gamma-1}M_{n_1}^2 - 1}} \qquad M_2 = \frac{M_{n_2}}{\sin(\beta - \theta)}$$

In the regions where a Prandtl-Meyer (P-M) expansion occurred, a number of steps were required. The P-M function was calculated for the region preceding the expansion using the following equation:

$$\nu(M) = \sqrt{\frac{\gamma+1}{\gamma-1}}\ \tan^{-1}\left(\sqrt{\frac{\gamma-1}{\gamma+1}(M^2-1)} - \tan^{-1}\sqrt{M^2-1}\right)$$

90

Knowing this value and the value for the turn angle of the expansion, the P-M function could be calculated for the region in question. $\nu(M_2) = \Delta\theta + \nu(M_1)$

A subroutine was written for the purpose of iterating on the P-M function equation in order to find the Mach number which corresponds to the value of the P-M function in that region. Using this Mach number, and the stagnation pressure found in the region before the expansion, the pressure could be calculated from the isentropic relation:

$$P = \frac{P_0}{\left(1 + \frac{\gamma-1}{2}M^2\right)^{\frac{\gamma}{\gamma-1}}}$$

Once the pressures on all faces were known, the forces acting on each section could be found. The forces were found by multiplying the pressure by the value of the area. The forces were then resolved into axial and normal forces referenced to the zero reference line. The normal and axial forces were then resolved into lift and drag forces by using the following equations:

$$Lift = Normal \cdot \cos\alpha - Axial \cdot \sin\alpha$$
$$Drag = Normal \cdot \sin\alpha + Axial \cdot \cos\alpha$$

The previous procedure was done for each of the cross sections, and the values of lift and drag for each section were summed. This total was doubled since the original calculations were only done for half of the aircraft. A loop was put in which ran the program for a variety of angles of attack. The lift and

91

drag coefficients, and the lift-to-drag ratios were also calculated and displayed.

Appendix C

Appendix C: Program CDHEAT

C.1 Overview:

The purpose of this program is to determine the aerodynamic heat flux to the surface of the waverider configuration. The program was base on "Conceptual Design Aerodynamic Heating Analysis" (CDHEAT) and various NASA technical reports (see References 12 and 13). When considering a hypersonic cruise vehicle, the heat flux is a function of angle of attack, Mach number, altitude, sweep angle, and both the leading edge and nose radii of curvature. This program has 4 objectives:

1.   To determine the heat flux at the stagnation point and line along the nose and leading edge of the aircraft.

2.   To determine the ratio of laminar heat flux to the stagnation heat flux behind the stagnation line.

3.   To determine the ratio of turbulent heat flux to a theoretical turbulent stagnation line.

4.   Determine the local skin temperature distribution utilizing known energy balance equations.

When determining the heat transfer coefficients, the worst possible case is assumed. This case corresponds to the top, or leeward, surface parallel to the free stream, and the bottom, or windward, surface at a 6.13 degree angle of attack.

The plane was divided into distinct entities, and the interference between these surfaces was ignored. The surfaces were defined as follows:

1. The nose cap.

2. The leading edge.

3. The top surface was modelled as a flat plat at zero angle of attack during laminar flow. For turbulent flow it was modelled as a delta wing at zero angle of attack.

4. The bottom surface was modelled as a delta wing at a 6.13 degrees angle of attack with a varying sweep angle, depending on the distance from the nose.

C.2   Laminar Heat Flux:

All laminar heat transfer coefficients were calculated using the method outlined in Reference 10, outlined as follows:

C.2.1   STAGNATION POINT

$$h_o = .1055 \left(P_\infty / P_{ATM} \right)^{.5} \left(V_\infty / 10^4 \right)^{1.16}$$

$$h_N = h_o / \sqrt{r_N}$$

C.2.2   STAGNATION LINE

$$h_{LE} = h_o \left[.72 \left(\cos \Lambda_{eff} \right)^{1.15} + .04 \sin \Lambda_{eff} \right] \left(P_f / r_{LE} \right)^{.5}$$

WHERE .....

$$\Lambda_{eff} = \sin^{-1} \left(\sin \Lambda \cos \alpha \right)$$

$$P_f = \frac{1.33 \left(M_\infty \cos \Lambda_{eff} \right)^2 + 1}{\left(1.33 M_\infty^2 + 2.5 \right) \left(\cos^2 \Lambda_{eff} + .0019 \right)}$$

C.2.3   FLAT PLATE (UPPER SURFACE)

$$h_{f_{PL}} = .00645 \left(\frac{P_\infty}{P_{ATM}} \right)^{.478} \left(\frac{V_\infty}{10^4} \right)^{1.42} \left[1 - .025 \left(\frac{10^4}{V_\infty} \right)^2 \right]$$

C.2.4   DELTA WING (UPPER SURFACE)

$$\frac{h_L}{h_0} = \frac{\left[P_f (1+2N)/3x \right]^{.5} \left(1.7 \sin\beta - .86\sin^2\beta + .036 \right)}{(M_\infty \sin\beta)^2 + 1}$$

WHERE....

$$N = \frac{.195 \sin d \tan \Lambda_{LE}}{(U_e/V_\infty)}$$

$$P_f \ (\text{given in } C.2.2)$$

C.3   Turbulent Heat Flux:

All turbulent heat transfer coefficients were calculated using the methods outlined in Reference 10, with some basis in References 12 and 13.

C.3.1   TURBULENT REFERENCE COEFFICIENT

$$h_{RT} = .437 \left(\frac{P_\infty}{P_{ATM}} \right)^{.78} \left(\frac{V_\infty}{10^4} \right)^{1.54}$$

C.3.2 DELTA WING (UPPER SURFACE)

$$\frac{h_T}{h_{RT}} = f(T_w)\left\{ (x/10)^{-2}\left[(1+1.25N)/2.25x\right]^{.2} P_f^{.8} \right.$$
$$\left. (2.9\sin^{1.5}\beta - 1.6\sin^{.3}\beta + .02)/([M_\infty\sin\beta]^2 + 1) \right\}$$

WHERE ....
$$f(T_w) = 1 - .00013(T_w - 1540)$$
$$N \text{ (given in C.2.4)}$$
$$P_f \text{ (given in C.2.2)}$$

C.3.3 DELTA WING (LOWER SURFACE)

$$\frac{h_T}{h_{RT}} = f(T_w)\left\{ (x/10)^{-2}\left[(1+1.25N)/2.25x\right]^{.2} P_f^{.8} \right.$$
$$\left. (2.9\sin^{1.5}\beta - 1.6\sin^{.3}\beta + .02)/([M_\infty\sin\beta]^2 + 1) \right\}$$

WHERE ....
$$f(T_w) \text{ (given in C.3.2)}$$
$$N \text{ (given in C.2.4)}$$
$$P_f \text{ (given in C.2.2)}$$

C.4 Skin Temperature Distribution:

The local skin temperature distribution was calculated by iteratively solving the energy balance equation:

$$\dot{q} = h(T_w - T_R) = \varepsilon \sigma T_w^4$$

C.5 Liquid Convection:

The average skin temperature was calculated by dividing the aircraft into 250 finite areas and determining the average temperature of each finite area. From these finite areas the flow rates and system weights can be calculated by the methods derived in References 12 and 13. The following is an outline of the equations used to calculate the required data:

$$\text{Coolant Flow Rate (lb/hr)} = \frac{h_i(T_R - T_w)(A_i) - \sigma \varepsilon T_w^4 A_i}{C_{Pc}(T_o - T_s)}$$

$$\text{Heat Exchanger Weight (lb)} = (5.75 \times 10^{-5})(CFR)(C_{Pc})(T_o - T_s)$$

$$\text{Hydrogen Flow Rate (lb/hr)} = \frac{CFR\left[(T_o - T_s)\,C_{Pc}\right]}{(C_{Pf})(370)}$$

$$\text{Distribution System Weight (lb)} = (.15\ \text{lb/ft}^2)(\Sigma A_i)$$

C.6   Tank Insulation; Carbon Dioxide Purge System:

Again an average skin temperature was determined by dividing the aircraft into 250 finite areas. In this case, however, the average temperature of both the front half of the plane (40 ft. from the nose) and the aft end of the aircraft (40 ft. to 75 ft.) was calculated. The weights and thicknesses were calculated by the methods outlined in References 13 and 16.

C.6.1   TOTAL WEIGHT OF THERMAL PROTECTION SYSTEM

$$W_{tpg} = \rho_i L + W_{Fg} + W_{fg}$$

C.6.2 AVERAGE FROST WEIGHT DURING FLIGHT

$$W_{Fg} = \frac{L^3 \rho_F{}^2}{t_1 B \rho_i (1+C)^3} \left[C(\eta_0 - \eta_1) + \frac{1+C}{2}(\eta_0{}^2 - \eta_1{}^2) - \frac{(1+C)^2}{3}(\eta_0{}^3 - \eta_1{}^3) \right.$$

$$\left. + \frac{C^2}{1+C} \ln \left\{ \frac{(1+C)\eta_0 - C}{(1+C)\eta_1 - C} \right\} \right]$$

WHERE....

$$C = k_{if}(T_S - T_f) / [k_i(T_b - T_S)]$$

$$B = k_i(T_b - T_S) / (\rho_i \Delta h_F)$$

C.6.3 TOTAL INSULATION THICKNESS

$$L = \frac{(1+C) \left\{ \frac{B \rho_i t_1}{\rho_F} \right\}^{1/2}}{\left[\eta_0 - \eta_1 - \frac{1+C}{2}(\eta_0{}^2 - \eta_1{}^2) + \frac{C}{1+C} \ln \left\{ \frac{(1+C)\eta_0 - C}{(1+C)\eta_1 - C} \right\} \right]^{1/2}}$$

WHERE....

C (given in C.6.2)

B (given in C.6.2)

C.6.4 WEIGHT OF HYDROGEN BOIL OFF

$$W_{fg} = \frac{\rho_F LC}{1+C} \frac{\Delta h_F}{\Delta h_f} \left[-(\eta_0 - \eta_1) + \frac{1}{1+C} \ln \left\{ \frac{(1+C)\eta_0 - C}{(1+C)\eta_1 - C} \right\} \right] - \frac{Q}{\Delta h_f A}$$

WHERE....

L (given in C.6.3)

C (given in C.6.2)

It must be noted, that for all cases a value of $\eta_1 = C/(1+C)$ was used since it represents an equilibrium thickness of frost where no sublimation is taking place and only heat transfer is occurring. Likewise, an equilibrium value of $\eta_0 = .55$ was used.